nature communications

Article

https://doi.org/10.1038/s41467-024-55658-0

Tumor microenvironment-responsive engineered hybrid nanomedicine for photodynamic-immunotherapy via multi-pronged amplification of reactive oxygen species

Received: 5 March 2024

Accepted: 19 December 2024

Published online: 06 January 2025

Check for updates

Jinglin Zou[1,5], Cong Jiang[2,5], Qiangsheng Hu[2,5], Xinlin Jia[3], Shuqi Wang[1], Shiyue Wan[2], Yuanqing Mao[3], Dapeng Zhang[1], Peng Zhang[2] ✉, Bin Dai[4] & Yongsheng Li[1,4] ✉

Reactive oxygen species (ROS) is promising in cancer therapy by accelerating tumor cell death, whose therapeutic efficacy, however, is greatly limited by the hypoxia in the tumor microenvironment (TME) and the antioxidant defense. Amplification of oxidative stress has been successfully employed for tumor therapy, but the interactions between cancer cells and the other factors of TME usually lead to inadequate tumor treatments. To tackle this issue, we develop a pH/redox dual-responsive nanomedicine based on the remodeling of cancer-associated fibroblasts (CAFs) for multi-pronged amplification of ROS (ZnPP@FQOS). It is demonstrated that ROS generated by ZnPP@FQOS is endogenously/exogenously multiply amplified owing to the CAFs remodeling and down-regulation of anti-oxidative stress in cancer cells, ultimately achieving the efficient photodynamic therapy in a female tumor-bearing mouse model. More importantly, ZnPP@FQOS is verified to enable the stimulation of enhanced immune responses and systemic immunity. This strategy remarkably potentiates the efficacy of photodynamic-immunotherapy, thus providing a promising enlightenment for tumor therapy.

Reactive oxygen species (ROS) is regarded as one of the main factors for tumor therapy, which maintains redox balance in tumor tissues[1]. Dynamic ROS-based cancer therapies are therapeutic modalities for endogenous/exogenous responsive ROS generation within tumors, including photodynamic therapy (PDT), sonodynamic therapy (SDT), chemodynamic therapy (CDT), etc. However, many cancer cells exhibit enhanced endogenous antioxidant capacity, allowing them to survive under the condition of sustained high levels of oxidative stress[2].

[1]Lab of Low-Dimensional Materials Chemistry, Key Laboratory for Ultrafine Materials of Ministry of Education, Frontier Science Center of the Materials Biology and Dynamic Chemistry, Shanghai Engineering Research Center of Hierarchical Nanomaterials, School of Materials Science and Engineering, East China University of Science and Technology, Shanghai, China. [2]Department of Thoracic Surgery, Shanghai Pulmonary Hospital, Tongji University School of Medicine, Shanghai, China. [3]Shanghai Key Laboratory of Orthopaedic Implants, Department of Orthopaedic Surgery, Shanghai Ninth People's Hospital, Shanghai Jiao Tong University School of Medicine, Shanghai, China. [4]Key Laboratory for Green Processing of Chemical Engineering of Xinjiang Bingtuan, School of Chemistry and Chemical Engineering, Shihezi University, Shihezi, China. [5]These authors contributed equally: Jinglin Zou, Cong Jiang, Qiangsheng Hu. ✉e-mail: zhangpeng1121@tongji.edu.cn; ysli@ecust.edu.cn

Specifically, intracellular antioxidant systems including antioxidant enzymes and antioxidants, such as glutathione (GSH)[3], heme oxygenase 1 (HO-1)[4], etc., consume large amounts of ROS, protect cellular active components from oxidation, and ultimately reduce ROS-mediated cellular damage[5]. Therefore, the therapeutic efficacy of general ROS-based cancer therapies would be significantly hindered. To address this issue, various nanomedicines capable of amplifying ROS from endogenous and exogenous perspectives have been developed[6–9]. Nevertheless, these nanomedicines are usually constrained by the interference among multiple ROS amplification pathways targeting only cancer cells as well as hypoxia condition, ultimately leading to unsatisfactory therapeutic effects. Therefore, a strategy of ROS amplification taking into account the synergistic interaction among different specific components in tumor microenvironment (TME) is intriguing and essential to be developed.

Cancer-associated fibroblasts (CAFs) are the predominant stromal cells, representing the major source of extra cellular matrix (ECM) components. They could promote tumor growth and mediate tumor chemoresistance as well as immune tolerance[10]. Since CAFs are perivascularly localized and the direct-action sites of tumor therapeutics after vascular extravasation, they are attractive targets for tumor treatment[11]. It is reported that activated CAFs and the ECM generated from CAFs are the key factors to lead high solid stress in the tumor during cancer progression, which compresses the tumor vessels, decreases blood perfusion, and thus reduces external oxygen supply[12–14]. Also, activated CAFs generate enormous contractile forces that constrict the ECM components[15,16]. Besides, CAFs secrete excessive amounts of ECM proteins, including collagen I and Collagen IV, which increase tissue volume and displace existing viscoelastic structures of the tumor tissue[17]. It is believed that modulation of CAFs would reduce the solid stress in tumors, improve the external oxygen delivery and feed ROS-based therapies, thereby substantially enhancing their therapeutic efficacy[18,19]. Currently, there are two main strategies to modulate CAFs: eliminating them and inducing them to be quiescent. It is worth noting that both strategies have their merits and demerits. Direct CAFs depletion has the potential to reduce the stromal barrier, limit tumor growth, and facilitate a second wave of therapy, but several studies have shown that indiscriminate killing of CAFs increases the risk of losing key stromal elements required for tissue homeostasis and instead accelerates tumor progression[20–23]. The heterogeneity of CAFs encompasses both cancer-supportive and cancer-inhibitory phenotypes, making CAFs depletion a double-edged sword[24]. Meanwhile, since quiescent fibroblasts can transdifferentiate into CAFs to drive the pro-fibro-proliferative response and tumor progression, reversing activated CAFs back to a quiescent phenotype would be a more promising approach to regulate ECM. Theoretically, the potential risk of this strategy is much lower than that of CAFs depletion. However, small molecules with the ability to induce quiescence of CAFs tend to have certain cytotoxicity, e.g., calcipotriol[25], JQ-1[26], all-trans retinoic acid[27–30], quercetin[31]. Meanwhile, the lack of controlled and specific drug release mode could cause systemic toxicity. Hence, it is imperative to develop a CAFs modulation-based strategy to circumvent the demerits of the above mentioned two strategies for tumor therapy.

Herein, we report a hybrid organosilica-based nanomedicine (ZnPP@FQOS) to remodel CAFs for achieving the multi-pronged ROS amplification therapeutic efficacy (Fig. 1a) by constructing TME responsive nanoparticle loaded with hydrophilic quercetin (Que) and hydrophobic photosensitizer zinc protoporphyrin (ZnPP), simultaneously. With the nanomedicine enriching at the tumor site, Que, transited from hydrophilic into hydrophobic feature owing to the weak acidity of TME, exudes firstly and would remodel CAFs by down-regulating various fibrosis-related factors, such as Wnt16, FAP-α, to bring them into quiescent state, thereby relieving hypoxia of TME and consequently amplifying the generated ROS (Fig. 1b). Then, Que entering tumor cells would generate ROS by inducing apoptosis. In the meantime, ZnPP encapsulated in the hydrophobic core is released triggered by the excess GSH in the tumor cells, so that PDT effect is activated with 660 nm laser irradiation and a large amount of $^1O_2$ is produced. Besides, ZnPP is able to down-regulate HO-1 marker, weakening the cellular anti-oxidative stress capacity. Consequently, the generated ROS is further amplified, ultimately realizing endogenous/exogenous multi-pronged ROS amplification (Fig. 1c). Benefiting from the CAFs remodeling and the administration of PDT, ZnPP@FQOS could induce systemic anti-tumor immune response and significantly inhibit tumor growth. More interestingly, by combining PDT with PD-L1 checkpoint blockade immunotherapy, the systemic immune response is thus enhanced, resulting in effective inhibition of primary and distant tumor growth in Pan02 tumor-bearing mice. This CAFs remodeling-based ROS amplification strategy pioneers an avenue for the development of enhanced PDT and PDT-immunotherapy.

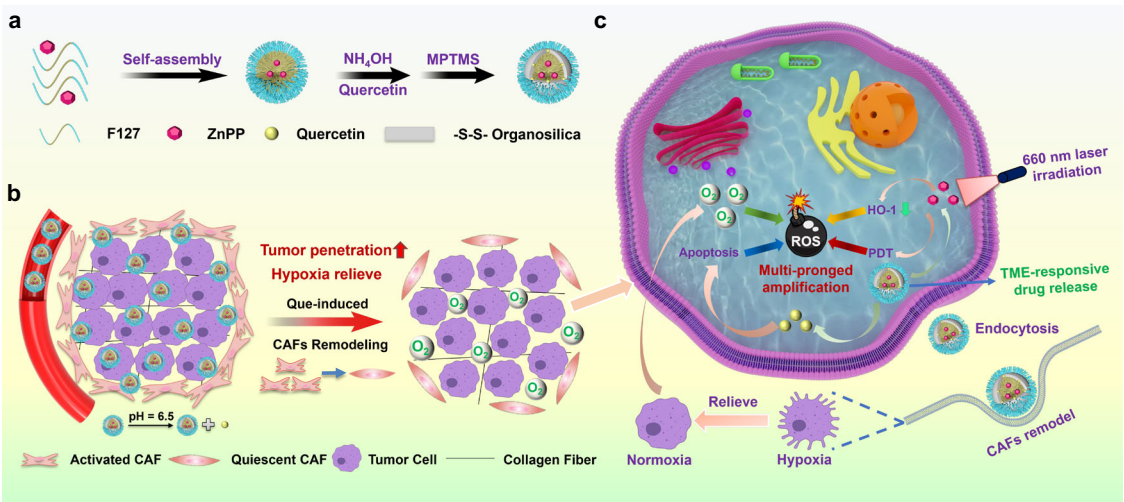

Fig. 1 | Schematic illustration of ZnPP@FQOS for the treatment of fibroblast-rich tumors by multi-pronged ROS amplification. a Schematic illustration of the synthesis of ZnPP@FQOS hybrid nanomedicine. **b** Delivery mechanism of ZnPP@FQOS in the tumor microenvironment by remodeling CAFs to enhance tumor penetration as well as its alleviation of hypoxia. **c** Cancer cell treatment mechanism by multi-pronged amplification of intracellular ROS induced by ZnPP@FQOS. MPTMS, (3-Mercaptopropyl)trimethoxysilane.

https://doi.org/10.1038/s41467-024-55658-0

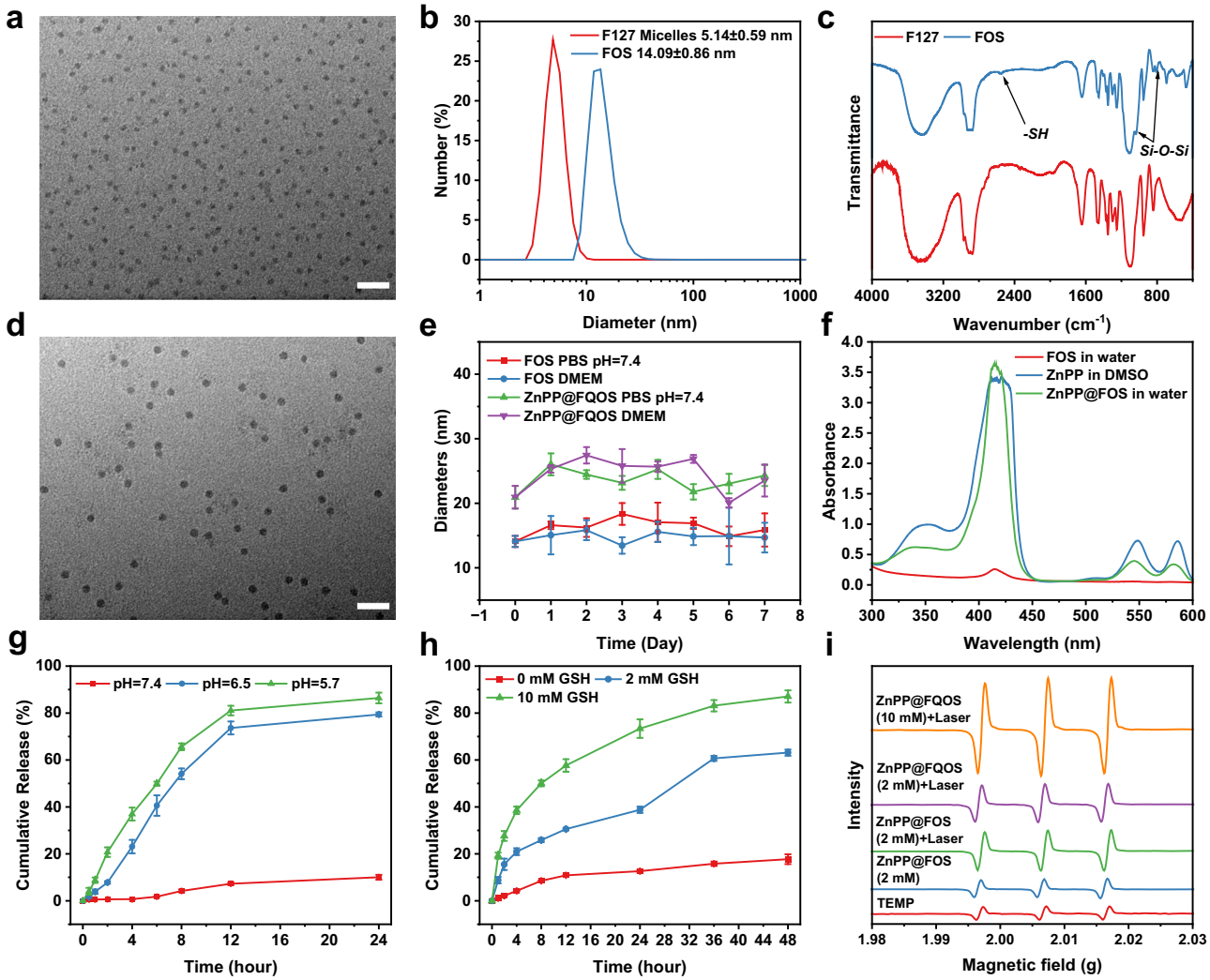

Fig. 2 | Characterizations of FOS and ZnPP@FQOS. a TEM image of FOS. (n = 3, independent samples) (scale bar: 50 nm) **b** Diameter distribution curves of F127 micelles and FOS. ($n = 3$ independent samples) **c** FT-IR spectra of F127 and FOS. **d** TEM image of ZnPP@FQOS. ($n = 3$ independent samples) (scale bar: 50 nm) (**e**) Stability of FOS and ZnPP@FQOS in PBS and DMEM for 7 days. ($n = 3$ independent samples) (**f**) UV-vis spectra of FOS, Free ZnPP and ZnPP@FOS. **g** Cumulative drug release curves of ZnPP@FQOS in PBS with different pH values. ($n = 3$ independent samples) **h** Cumulative drug release curves of ZnPP@FQOS in PBS (pH=7.4) containing different concentrations of GSH. ($n = 3$ independent samples) **i** ESR spectra of pure TEMP, ZnPP@FOS and ZnPP@FQOS under 660 nm laser irradiation (300 mW cm^{-2}). Data are presented as means ± SD. Source data are provided as a Source Data file.

Results

Characterizations of FOS and ZnPP@FQOS

The organosilica-based hybrid micelle (FOS) with uniform particle size was synthesized by a method similar to that reported in the previous studies[32–34]. As shown in Fig. 2a, FOS presents spherical morphology based on the transmission electron microscopy (TEM) images, and a narrow polydisperse size of 14.09 ± 0.86 nm according to the dynamic light scattering (DLS) analysis results (Fig. 2b). The introduction of -SH groups on the surface of the cross-linked network formed by MPTMS resulted in an electronegativity of −8.15 ± 1.40 mV for FOS (Supplementary Fig. 1). The appearance of peaks at 800 cm^{-1} and 1110 cm^{-1} in the Fourier transform infrared (FT-IR) spectra (Fig. 2c), corresponding to the Si-O-Si bond stretching vibration, indicates the successful formation of a cross-linked silica network between the PEO and PPO segments of the micelles during the preparation of FOS[32,35]. Furthermore, the peak at 510 cm^{-1} in the Raman spectra attributed to the S-S group, along with the peak at 2550 cm^{-1} in both the FT-IR and Raman spectra, corresponding to the -SH bond, confirms the conversion of sulfhydryl groups to disulfide bonds in the silica-based shell through an oxidation reaction. (Fig. 2c and Supplementary Fig. 2). The redox behavior of FOS was investigated through co-incubating it with PBS buffer containing different concentrations of GSH. TEM images reveal the complete degradation of FOS after 5 days of incubation, indicating the strong responsiveness of FOS to GSH (Supplementary Fig. 3).

After loading with ZnPP and Que, ZnPP@FQOS maintains the narrow polydispersity and the spherical morphology (Fig. 2d). DLS analysis results reveal no significant change in the particle size of the nanomedicine after loading ZnPP and Que, respectively, and a slight increase of the particle size to 24.86 ± 0.78 nm (Supplementary Fig. 4) is observed after co-loading, with no distinct difference in the Zeta potential profile (Supplementary Fig. 5). Both FOS and ZnPP@FQOS demonstrate favorable stability in various media, owing to the organosilica hybrid networks (Fig. 2e). Compared to free ZnPP, absorption peaks at 545 nm and 585 nm in UV-vis absorption spectra are detected for ZnPP@FOS (Fig. 2f). Similarly, FQOS exhibits an absorption peak at 315 nm compared to free Que (Supplementary Fig. 6). These confirm the successful loading of ZnPP and Que into ZnPP@FQOS. Furthermore, according to the standard curves of free ZnPP and Que in UV-vis spectra, the drug encapsulation efficiency (EE) of ZnPP and Que, calculated by Eq. (1), is found to be 50.10% and 64.84%, respectively, and

the drug loading capacity (LC) of ZnPP and Que, calculated by Eq. (2), is 0.91% and 1.17%, respectively (Supplementary Figs. 7, 8). In order to investigate the in vitro drug release profiles of the nanomedicine, ZnPP@FQOS was incubated in PBS buffer with varied pH values and GSH concentrations. The release of Que in PBS at pH=6.5 and pH=5.7 reach 79.41% and 86.43%, respectively, after 24 h, substantially higher than the release observed in PBS at pH=7.4 (Fig. 2g). Meanwhile, the release of ZnPP in PBS containing 10 mM GSH reaches 87.07% after 48 h, which is considerably higher than the release observed in PBS without GSH (Fig. 2h). These results suggest that ZnPP@FQOS holds great potential for selectively releasing ZnPP and Que in response to the mildly acidic pH and elevated GSH levels commonly found in the TME. To further clarify the release profiles of ZnPP and Que in the TME, we conducted comprehensively evaluations of the release behavior of the two drugs at different pH and GSH concentrations. The results show that the cumulative release rates of ZnPP and Que are 73.65% and 91.25%, respectively, at GSH = 10 mM and pH=5.7 (Supplementary Fig. 9a). At GSH = 10 mM and pH = 6.5, the cumulative release rates of ZnPP and Que are 73.54% and 85.06%, respectively (Supplementary Fig. 9b). Overall, the release behavior of ZnPP is slower than that of Que over the 24-hour period, which ensures the sustained photodynamic therapeutic effect of the nanomedicine. Moreover, the pH value has a relatively minor effect on the release of Que (Supplementary Fig. 9a–c), which is mainly due to the destructive effect of GSH to the silica-based shell layer. The release profile of ZnPP is dependent on the intracellular GSH concentration. To investigate this, we measured the GSH levels in different cell types and found that the GSH concentration in cancer cells is considerably higher than that in fibroblasts (Supplementary Fig. 10). Hence, when ZnPP@FQOS is internalized by CAFs, the release of ZnPP is considered to be slower, resulting in a weaker PDT effect upon laser irradiation, with less impact on the cell viability of CAFs. Then, the capability of ZnPP@FQOS to generate $^1O_2$ under 660 nm laser irradiation was evaluated via an electron spin resonance (ESR) spectrometer (Fig. 2i). By using TEMP as a trapping agent for $^1O_2$, the nanomedicine displays 1:1:1 signal pattern upon laser irradiation, with the signal intensity increasing as the ZnPP concentration is raised. This confirms that ZnPP@FQOS possesses the satisfactory capability to produce $^1O_2$ in vitro. Additionally, it was further validated by the UV-vis absorption changes before and after the reaction of DPBF with $^1O_2$ (Supplementary Fig. 11).

$$EE = \frac{W_{drug\ in\ samples}}{W_{drug\ feeded}} \times 100\% \quad (1)$$

$$LC = \frac{W_{drug\ in\ samples}}{W_{FOS}} \times 100\% \quad (2)$$

In vitro cellular uptake and tumor penetration ability of ZnPP@FQOS

The cellular uptake behavior was investigated by confocal laser scanning microscopy (CLSM) by incubating ZnPP@FQOS with Pan02 cells and TGF-β activated 3T3 cells for different periods. The red fluorescence of ZnPP@FQOS around the Pan02 cells became brighter as the incubation time is prolonged, indicates its continuous cellular uptake process. In addition, there is no significant difference in the fluorescence intensity between 8 and 12 h, suggesting that the uptake of ZnPP@FQOS by Pan02 cells reaches saturation at 8 h (Fig. 3a and Supplementary Fig. 12). Since fibroblasts in the TME are mostly activated, the cellular uptake behavior of TGF-β-activated 3T3 cells was also evaluated. The results show a similar cellular uptake ability as Pan02 cells, and cellular uptake reach saturation at 8 h, demonstrating that nanomedicines could also be uptaken by CAFs in the TME (Fig. 3b and Supplementary Fig. 13). Besides, flow cytometry was used as a further quantitative assessment of ZnPP@FQOS tumor cellular uptake capacity (Supplementary Fig. 14), and the results demonstrate a similar trend to the mean fluorescence intensity. In order to explore the cellular uptake properties of nanomedicines more comprehensively, the cellular uptake capacity of different nanomedicines was also evaluated by CLSM after co-incubating Pan02 or TGF-β activated 3T3 cells with Free ZnPP; ZnPP@FOS; ZnPP@FOS+Free Que and ZnPP@FQOS for 4 h, respectively (Supplementary Figs. 15, 16), and also quantified the mean fluorescence intensity (Supplementary Figs. 17, 18). It is showed that the fluorescence intensity of the free ZnPP group is slightly higher than that of the other three groups, and no significant difference is observed between the fluorescence intensities of the three groups of nanomedicines, which is probably due to the fact that free drugs tend to be uptaken more quickly by cells in vitro.

In addition, due to the presence of a large number of CAFs in the tumors, multicellular tumor spheroids (MCTS) were generated as a model by co-mixing KP cells and TGF-β-activated 3T3 cells to better mimic the complex composition in the TME. According to the CLSM images of different treatment groups (Fig. 3c and Supplementary Figs. 19, 20), ZnPP@FQOS easily diffuses from the surface to the inner core of the MCTS in the range of 70 μm with pH=6.5. In contrast, the fluorescence of the group without Que is distributed only superficially, and the depth of the fluorescence signal is also shallow in the mixed Que group as well as in the ZnPP@FQOS (pH=7.4) group, which further emphasizes the importance of the pH-responsive release property of Que loaded in the organosilica cross-linking shell layer for the remodeling of CAFs in the TME and the efficient drug delivery to the deep tumor tissues.

In vitro potency of ZnPP@FQOS to multi-pronged ROS amplification

Firstly, the capability of ZnPP@FQOS to trigger the remodeling of CAFs in vitro was evaluated in a weakly acidic environment at pH=6.5. It is reported that Wnt16 plays an important role in stroma restructuring and CAFs quiescence, and Que is capable to regulate the Wnt16 expression[36], and some fibrotic markers are also affected, including FAP-α, α-SMA and Collagen. As shown in Fig. 4a, the FQOS, ZnPP@FQOS, and ZnPP@FQOS+Laser groups significantly reduce the expression of Wnt16, FAP-α, Collagen I, Collagen IV, and α-SMA in TGF-β-activated 3T3 cells, and the expression levels are close to those of the negative control group. However, the ZnPP@FOS group hardly downregulates the expression of related markers. A similar phenomenon is observed in the immunofluorescence analysis (Fig. 4b and Supplementary Fig. 21), where ZnPP@FQOS and ZnPP@FQOS+Laser group considerably reduce the expression of α-SMA. Therefore, ZnPP@FQOS is effective in reducing CAF phenotype and ECM assembly, suggesting its potential to remodel the immunosuppressive microenvironment in vivo. In addition, Que has been reported to downregulate the apoptosis-related markers such as Bcl-xL by causing apoptosis pathways and thus generating ROS[37]. As shown in Supplementary Fig. 23, Bcl-xL expression in KP cells is significantly reduced by Que-containing FQOS, ZnPP@FQOS and ZnPP@FQOS+Laser groups, demonstrating that ZnPP@FQOS could generate ROS via the apoptosis pathway. HO-1 is an antioxidant enzyme that plays a pivotal role in ROS scavenging. ZnPP has been reported to be a potent HO-1 inhibitor, which is owing to ZnPP is a heme derivative and can more competitively bind to the active site of HO-1 enzyme than heme[38–41]. As shown in Fig. 4a, HO-1 protein expression is remarkably reduced in the ZnPP@FOS, ZnPP@FQOS, and ZnPP@FQOS+Laser groups compared to the ROS-positive group. Meanwhile, immunofluorescence analysis further confirms that ZnPP@FQOS could reduce HO-1 expression (Fig. 4c and Supplementary Fig. 22). Intracellular $^1O_2$ was observed with SOSG, and green fluorescence of SOSG is observed in ZnPP@FOS and ZnPP@FQOS cultured KP and 3T3 mixed cells after 660 nm laser irradiation (Fig. 4d), which indicates that ZnPP promoted $^1O_2$ production under laser irradiation though a PDT effect. In order to evaluate

https://doi.org/10.1038/s41467-024-55658-0

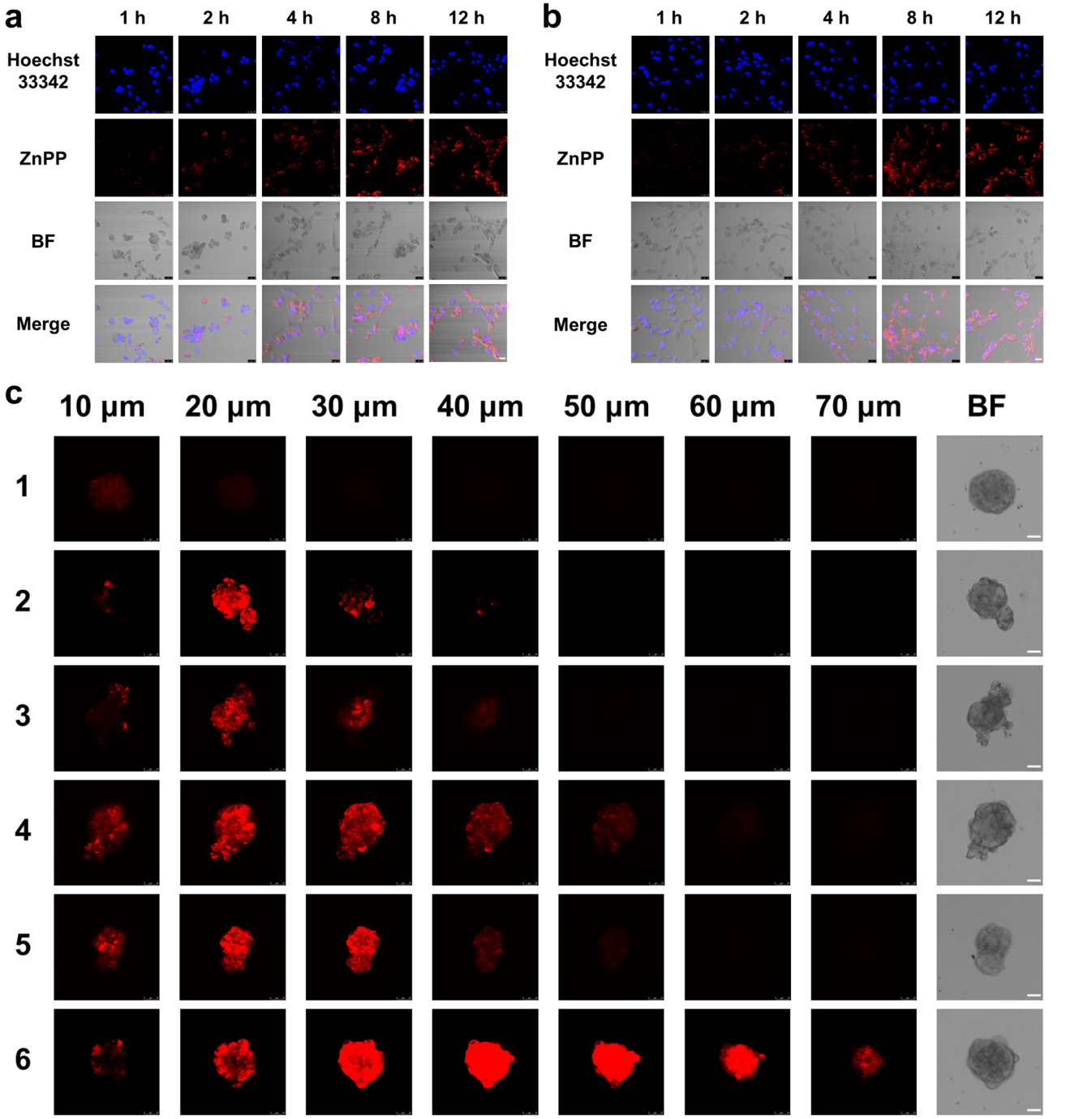

Fig. 3 | Cellular uptake and tumor penetration ability of ZnPP@FQOS. CLSM images of (**a**) Pan02 cells and (**b**) TGF-β-activated 3T3 cells incubated with ZnPP@FQOS for various periods. (ZnPP dose: 7.724 mg/L, scale bar: 25 μm) (1×10^5 cells/mL, n = 3 independent biological samples) (**c**) CLSM images showing the MCTS penetration depth. (1:Free ZnPP; 2:ZnPP@FOS; 3:ZnPP@FOS pH=6.5; 4:ZnPP@FOS+Free Que; 5:ZnPP@FQOS; 6:ZnPP@FQOS pH=6.5, ZnPP dose: 7.724 mg/L; scale bar: 25 μm) (4×10^3 cells/mL, n = 3 independent biological samples). BF, bright field.

the total amount of intracellular ROS more intuitively, we used DCFH-DA to monitor the ROS level in KP and 3T3 mixed cells. As shown in Fig. 4e, ZnPP@FOS+Laser group shows a certain intensity of fluorescence due to the photodynamic as well as HO-1 down-regulation effect triggered by ZnPP. Since the monolayer cells could not mimic the state of the TME well, FQOS group only shows weak fluorescence due to Que-induced apoptosis, while the ZnPP@FQOS group shows stronger fluorescence than the FQOS group due to the stronger HO-1 down-regulation effect. The green fluorescence in ZnPP@FQOS+Laser group is the most prominent due to a combination of the photodynamic effect, HO-1 down-regulation effect induced by ZnPP and Que-induced apoptosis. In addition, we analyzed mitochondrial function by the JC-1 kit (Fig. 4f). Red fluorescent j-aggregates indicate normal mitochondria and green fluorescent j-monomers indicate decreased mitochondrial membrane potential. ZnPP@FQOS+Laser group shows the most severe mitochondrial damage effect, suggesting that the large amount of generated ROS triggers an abnormal mitochondrial membrane potential. These results preliminarily validate the feasibility of our strategy based on multi-pronged ROS amplification by remodeling CAFs.

https://doi.org/10.1038/s41467-024-55658-0

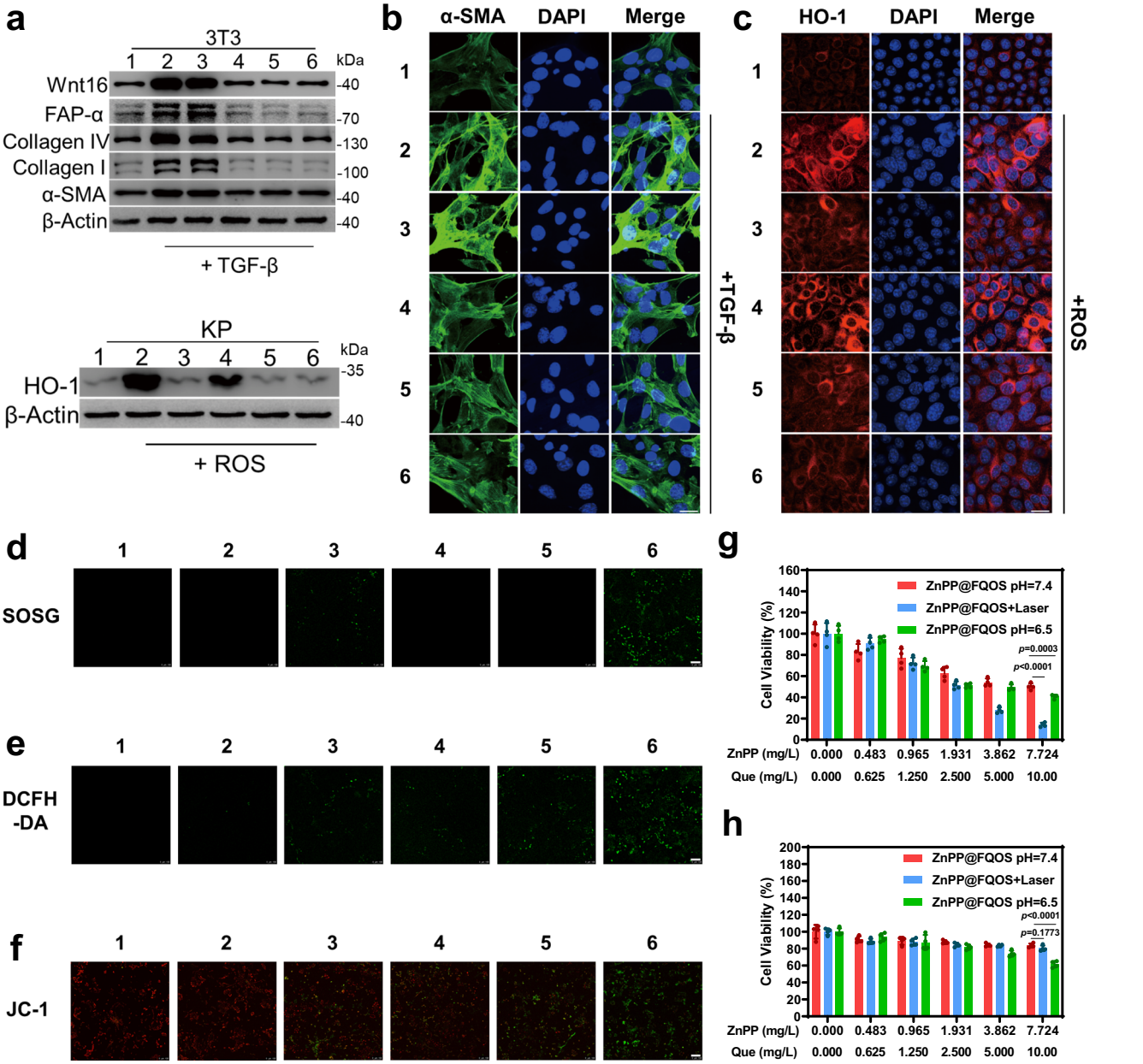

Fig. 4 | In vitro potency of ZnPP@FQOS to multi-pronged ROS amplification and cellular cytotoxicity. a Western blots of protein expression for Wnt16, FAP-α, Collagen IV, Collagen I and α-SMA of 3T3 cells at pH=6.5 under different treatments (1:TGF-β negative; 2: TGF-β positive; 3:ZnPP@FOS; 4:FQOS; 5:ZnPP@FQOS; 6:ZnPP@FQOS+Laser) and protein expression for HO−1 of KP cells under different treatments. (1:Control; 2:ROS up; 3:ZnPP@FOS; 4:FQOS; 5:ZnPP@FQOS; 6:ZnPP@FQOS+Laser) (1×10^5 cells/mL, $n = 3$ independent biological samples) (**b**) Immunofluorescence for α-SMA of 3T3 cells at pH=6.5 under different treatments. (1:TGF-β negative; 2: TGF-β positive; 3:ZnPP@FOS; 4:FQOS; 5:ZnPP@FQOS; 6:ZnPP@FQOS+Laser; scale bar: 10 μm) (5×10^4 cells/mL, $n = 3$ independent biological samples) (**c**) Immunofluorescence for HO-1 of KP cells under different treatments. (1:Control; 2:ROS up; 3:ZnPP@FOS; 4:FQOS; 5:ZnPP@FQOS; 6:ZnPP@FQOS+Laser; scale bar: 10 μm) (5×10^4 cells/mL, $n = 3$ independent biological samples) (**d**) CLSM images of KP and 3T3 mixed cells under different treatments and treated with SOSG probe. (scale bar: 100 μm) (1×10^5 cells/mL, $n = 3$ independent biological samples) (**e**) CLSM images of KP and 3T3 mixed cells under different treatments and treated with DCFH-DA probe. (scale bar: 100 μm) (1×10^5 cells/mL, $n = 3$ independent biological samples) (**f**) CLSM images of KP and 3T3 mixed cells mitochondrial membrane potential changes. (scale bar: 100 μm) (1×10^5 cells/mL, $n = 3$ independent biological samples) (1:Control; 2:ZnPP@FOS; 3:ZnPP@FOS+Laser; 4:FQOS; 5:ZnPP@FQOS; 6:ZnPP@FQOS+Laser) (ZnPP dose: 7.724 mg/L, Que dose: 10 mg/L) Cell viability of ZnPP@FQOS pH=7.4, ZnPP@FQOS +Laser, ZnPP@FQOS pH=6.5 for (**g**) KP cells and (**h**) 3T3 cells (5×10^4 cells/mL, $n = 4$ independent biological samples). Wnt16, Wingless / Integrated 16; FAP-α, Fibroblast activation protein-α; α-SMA, α-smooth muscle actin; TGF-β, Transforming growth factor-β; DAPI, 4′,6-Diamidino-2-Phenylindole Dihydrochloride; SOSG, Singlet Oxygen Sensor Green reagent; DCFH-DA, 2′,7′-Dichlorodihydrofluorescein Diacetate. Data are presented as means ± SD. Statistical significance was determined using two-tailed Student's t-test for pairwise comparisons, and one-way ANOVA analysis of variance for multiple groups. p values > 0.05 were considered non-significant, p values < 0.05 were considered statistically significant. Source data are provided as a Source Data file.

In vitro cellular cytotoxicity of ZnPP@FQOS

The cytotoxicity of ZnPP@FQOS was then examined by a cell counting method. Firstly, the cytotoxicity of FOS was evaluated. As shown in Supplementary Fig. 24, the cell viability of FOS for KP, Pan02, 3T3, and MEF cells maintain above 80%, which proves that nanocarriers had less effect on cytotoxicity. In the case of KP cells, the cell viability at pH=7.4 and pH=6.5 maintain 50.23% and 40.72%, respectively, after their incubation with Que (10 mg/L) and ZnPP (7.724 mg/L) loaded

nanomedicine. The cells only show 14.19% viability when further irradiated by laser (Fig. 4g). Meanwhile, the cytotoxicity of nanomedicine shows a dose-dependent behavior. For cell viability of Pan02 cells, (Supplementary Fig. 25), our nanomedicine shows a similar pattern. All these results tentatively demonstrate that ZnPP@FQOS has favorable cytotoxicity under laser irradiation. As shown in Fig. 4h and Supplementary Fig. 26, regardless of laser irradiation, 3T3 and MEF cells maintain high cell viability, however, the cell viability decreases to about 60% at pH=6.5, which preliminarily demonstrates that ZnPP@FQOS is slightly cytotoxic to fibroblasts in vitro under weakly acidic conditions and possibly induces a certain amount of apoptosis of CAFs in TME. In addition, flow cytometry was analyzed for in vitro apoptosis detection in KP cells under different culture conditions. As shown in Supplementary Fig. 27, the ZnPP@FQOS+Laser group shows a higher late apoptosis rate of 45.8%, and the ZnPP@FOS+Laser, FQOS, or ZnPP@FQOS group present a certain extent of late apoptosis. Furthermore, the cytotoxicity of nanomedicines is visually evaluated by a live/dead cell staining method (Supplementary Fig. 28). ZnPP@FQOS+Laser group exhibits the most pronounced cell death, which is consistent with the flow cytometry analysis. These results demonstrate that the generated ROS could cause high cytotoxicity on tumor cells, which match well with the ROS evaluation and suggest that ZnPP@FQOS could kill tumor cells effectively and achieve CAFs remodeling. In order to determine that multi-pronged amplification of ROS is the main cause of cell killing, we incubated KP cells with different nanomedicines and pretreated them with N-Acetyl-L-cysteine (NAC) to scavenge the ROS that generated and amplified by the multi-pronged ROS modulation strategy, then performed live-dead cell staining (Supplementary Fig. 29). It is showed that the tumor inhibition effect is attenuated, further illustrating that the multi-pronged ROS amplification strategy has a promising cell killing effect. The ability of multi-pronged ROS amplification to mediate DC2.4 cells maturation and thus influence immune activation was then studied. As shown in Supplementary Figs. 30, 31, ZnPP@FQOS+Laser group exhibits a higher number of DC2.4 cells maturation than other groups, which is owing to the significant immunogenic cell death (ICD) effect by PDT as well as CAFs remodeling.

In vivo biosafety and distribution of ZnPP@FQOS

Before in vivo tumor therapy study, the biosafety of ZnPP@FQOS was evaluated in healthy female C57BL/6 mice. Mice were injected with 10 mg/kg ZnPP@FQOS intravenously. There is no distinct difference in body weight between ZnPP@FQOS and control groups during the 18 days healthy observation (Supplementary Fig. 32). The blood indexes and liver&kidney function of the ZnPP@FQOS group are not considerably different from those of the control group (Supplementary Figs. 33, 34). In addition, hematoxylin & eosin (H&E) staining of major organs (heart, liver, spleen, lung, kidney) shows no significant damage in both groups (Supplementary Fig. 35). All these results prove that ZnPP@FQOS had good biocompatibility.

To evaluate the effect of Que treatment on nanomedicine delivery and CAFs remodeling efficiency, we performed in vivo fluorescence imaging on free ZnPP, ZnPP@FOS and ZnPP@FQOS treated tumor-bearing mice after intravenous injection, respectively. KP cells were co-mixed with TGF-β-activated 3T3 cells at a ratio of 3:1, which were injected subcutaneously into mice to establish a tumor-bearing mouse model. As shown in Fig. 5a, b, in free ZnPP group, the fluorescence accumulation reaches a maximum at 9 h, after which free ZnPP is rapidly eliminated in vivo, and there is no more significant fluorescence accumulation at 36 h, and the time-dependent fluorescence accumulation of ZnPP@FOS is detected at the tumor site within 36 h post-injection due to the enhanced permeability and retention effects, indicating that the delivery efficiency of ZnPP is efficiently increased by FOS. Surprisingly, compared to the ZnPP@FOS group, the ZnPP@FQOS group shows stronger fluorescence signal at the tumor site, indicating that Que-induced remodeling of CAFs effectively promotes nanomedicine delivery, penetration, and retention within the tumor. Ex vivo fluorescence quantitative imaging of major organs and tumors extracted from mice at 36 h post-injection also demonstrate significantly enhanced accumulation, penetration and retention of ZnPP@FQOS in tumors (Fig. 5c, d), with the ZnPP@FQOS group showing higher delivery efficiency than free ZnPP at 36 h post-injection. Meanwhile, the delivery efficiency is improved by 1.84 times compared with the ZnPP@FOS group. In addition, there is a preferential uptake of ZnPP@FQOS by liver, which is owing to the remodeling of CAFs that the interstitial fluid pressure of the tumor was reduced, the tumor tissue aggregation and infiltration ability is thus enhanced, so that the penetration of ZnPP@FQOS into deeper tissues is enabled. Generally, the enhanced accumulation and penetration of nanomedicines in tumor tissues render their exocytosis out of the tumor through the blood circulation more difficult, which, in turn, result in a delayed clearance effect to the nanomedicines in the metabolic organs represented by the liver. Consequently, after 36 h metabolism process, compared with the other groups, the fluorescence intensity of the ZnPP@FQOS treatment is still stronger in the liver. The results are consistent with the previously reported works[42–46]. Furthermore, we validated the CAFs remodeling effect of ZnPP@FQOS by intratumoral penetration assays. As shown in Fig. 5e and Supplementary Fig. 36, the fluorescence intensity of the nanomedicine was studied at the surface (0 mm) and at depth (3 mm) of the tumor after staining the blood vessels with CD31 antibody. It is observed that the fluorescence of the Free ZnPP group is mainly distributed on the surface of the tumor, with only a small amount going into the depths, and a part of the fluorescence of the ZnPP@FOS group appears in the depths, while there is a significant accumulation of fluorescence in the depths of the ZnPP@FQOS group. In addition, the fluorescence of the tumors in the Free ZnPP and ZnPP@FOS groups is mainly distributed in the perivascular area compared with that in the ZnPP@FQOS group. These suggest that CAFs remodeling played an important role in depth of tissue penetration and vascular extravasation.

In vivo photodynamic therapy and immune response of ZnPP@FQOS

ZnPP@FQOS displays satisfactory in vitro cytotoxicity by effectively inducing multi-pronged ROS amplification and good in vivo biosafety. We then evaluated the in vivo therapeutic effect of nanomedicines by establishing fibroblasts-rich KP tumor model, the procedure of which is shown in Fig. 6a. During the 18 days treatment period, the tumor volumes and body weights of the mice were measured every 3 days. As shown in Fig. 6b, compared with the rapid tumor growth in the control group, the remaining groups show tumor inhibition with different degrees. Among them, ZnPP@FQOS+Laser group shows the most obvious tumor inhibition effect with an inhibition rate of 92.9%. Besides, the tumor is weighed and the mass showed a similar trend to the volume (Supplementary Fig. 37). Digital photographs of tumors excised from mice further confirm the significant tumor suppression after ZnPP@FQOS+Laser treatment (Fig. 6c), and the significant therapeutic effect of nanomedicines on tumor tissues are simultaneously confirmed by hematoxylin and eosin (H&E) staining of tumor tissues, Ki-67 immunohistochemical staining and transferase-mediated dUTP nick end labeling (TUNEL) staining (Fig. 6d and Supplementary Fig. 38). All these results suggest that the strategy of multi-pronged amplification of ROS achieve impressive in vivo efficacy and could suppress tumor progression to a great extent. The body weights, blood indexes and liver&kidney function of the other five groups treated with corresponding nanomedicines remain similar to the control group (Supplementary Figs. 39–41). Meanwhile, H&E-stained images also show no significant damage to major organs in any of the five groups treated with nanomedicine (Supplementary Fig. 42). These indicate the importance of nanocarriers for encapsulation and delivery of free drugs.

https://doi.org/10.1038/s41467-024-55658-0

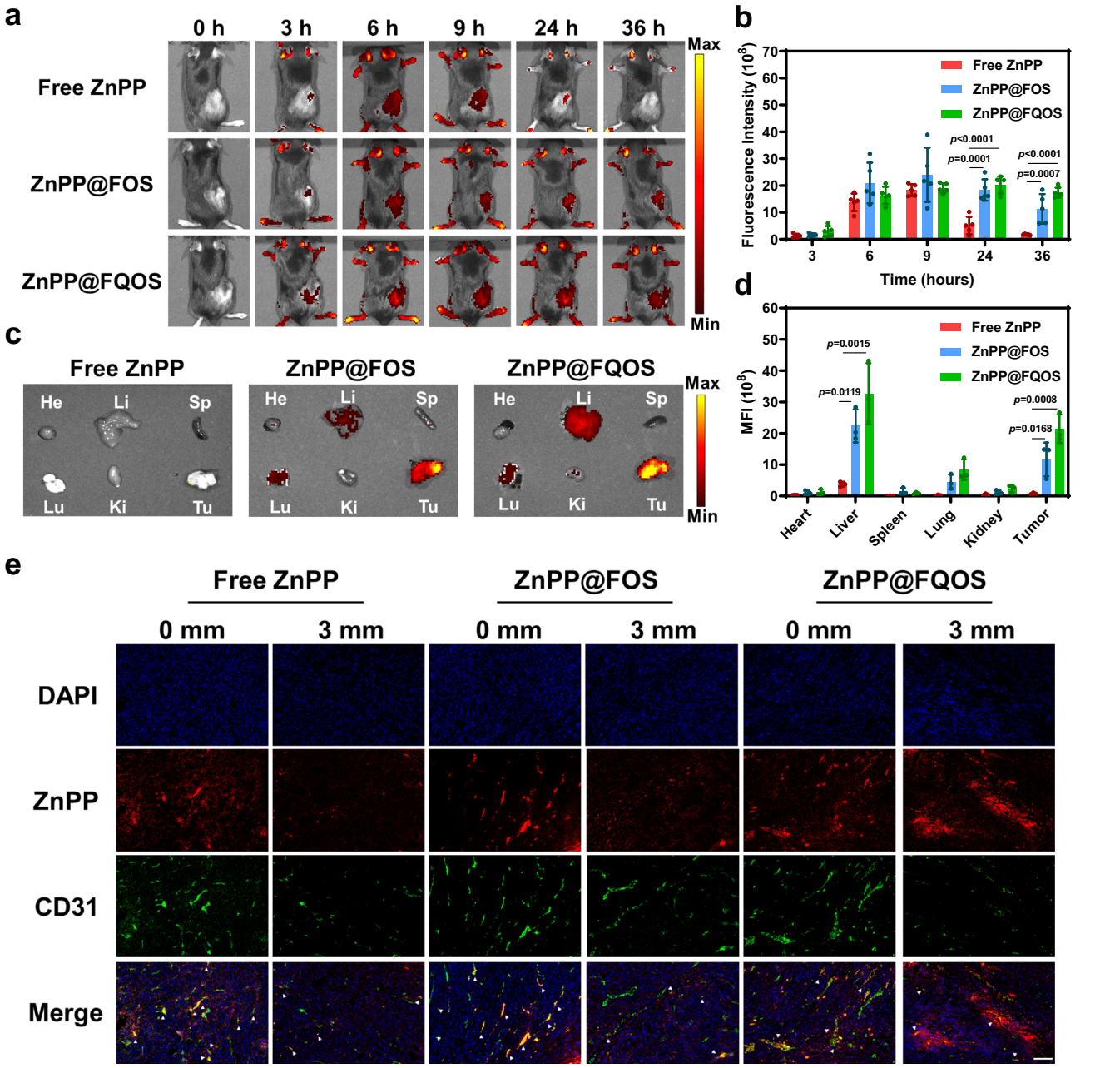

Fig. 5 | In vivo distribution of ZnPP@FQOS. a The in vivo fluorescence images of fibroblasts-rich KP tumor-bearing mice after the intravenous injection of nanomedicines at different times. (ZnPP dose: 3.862 mg/kg) **b** Mean fluorescence intensity of the tumor at different time points. (n = 5 independent biological samples) **c** The ex vivo fluorescence images of the major organs (heart, liver, spleen, lung, kidney) and tumors at 36 h after intravenous injection. **d** Mean fluorescence intensity of the major organs and tumors at 36 h. (n = 3 independent biological samples) **e** In vivo penetration experimental results of nanomedicines at the tumor surface (0 mm) and depth (3 mm). (scale bar: 100 μm) (n = 3 independent biological samples) He, heart; Li, liver; Sp, spleen; Lu, lung; Ki, kidney; Tu, tumor; MFI, mean fluorescence intensity; CD31, the differentiation of cluster 31. Data are presented as means ± SD. Statistical significance was determined using two-tailed Student's t-test for pairwise comparisons, and one-way ANOVA analysis of variance for multiple groups. p values > 0.05 were considered non-significant, p values < 0.05 were considered statistically significant. Source data are provided as a Source Data file.

The high efficacy of ZnPP@FQOS may be attributed to the following factors: 1) Que-induced remodeling of CAFs resulting in the relieving of TME hypoxia; 2) Que-mediated apoptosis; 3) down-regulation of HO-1 by ZnPP to disrupt the anti-oxidative stress defense and 4) production of $^1O_2$ by ZnPP under 660 nm laser irradiation, which ultimately results in a four-pronged amplification of intratumoral ROS. Firstly, to evaluate CAFs remodeling efficacy, western blotting, immunofluorescence and masson's trichrome staining analyses of HIF-1α, CAF prominent phenotypes (α-SMA and FAP-α), collagen and Wnt16 treated with different nanomedicines were performed. As shown in Fig. 6e, the expression of the above proteins is significantly reduced in Que-doped groups (4: FQOS; 5: ZnPP@FQOS; 6: ZnPP@FQOS+Laser). Meanwhile, red fluorescent HIF-1α and α-SMA are observed in immunofluorescence, and blue-labeled collagen in Masson's trichrome staining is substantially reduced in the FQOS, ZnPP@FQOS, ZnPP@FQOS+Laser groups (Fig. 6d and Supplementary Fig. 38). Then, western blotting of Bcl-xL is used to assess Que-mediated apoptosis (Fig. 6e). It is found that its expression in FQOS, ZnPP@FQOS, ZnPP@FQOS+Laser groups are remarkably decreased. Furthermore, the anti-oxidative stress level is evaluated by western

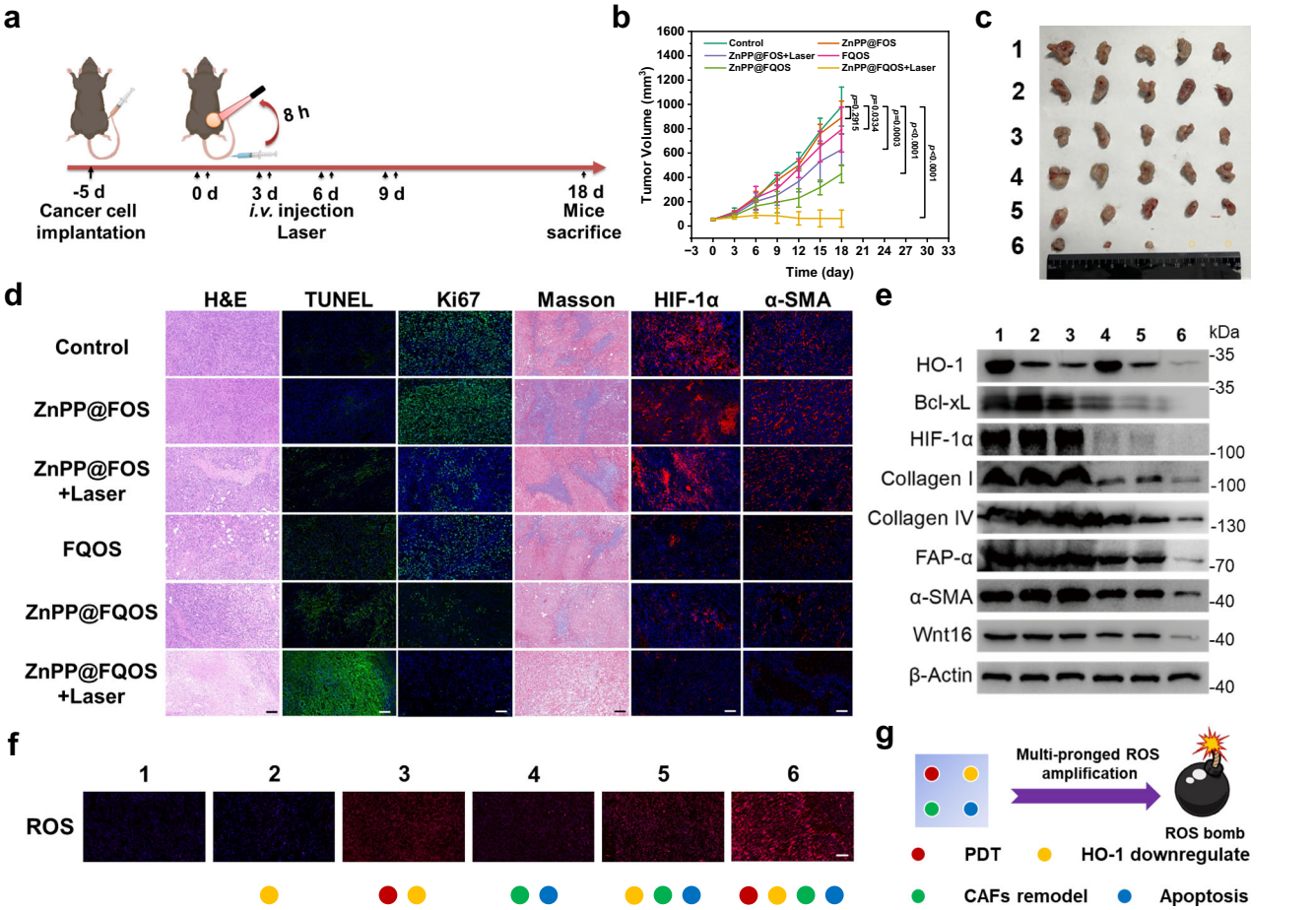

Fig. 6 | In vivo photodynamic therapy of ZnPP@FQOS for fibroblasts-rich KP tumor. a Schematic illustration of the treatment in fibroblasts-rich KP tumor models. **b** Tumor growth curves for different treatment groups. (n = 5 independent biological samples) (**c**) Photograph of the dissected tumors from each group after treatment. **d** H&E, TUNEL, Ki67, Masson's trichrome, HIF-1α and α-SMA staining of dissected tumors from each group. (scale bar: 50 μm) (n = 3 independent biological samples) (**e**) Western blotting analysis of HO−1, Bcl-xL, HIF-1α, Collagen I, Collagen IV, FAP-α, α-SMA and Wnt16 after the treatment of various formulation. (n = 3 independent biological samples) (**f**) DCFH-DA-stained tumor tissue sections from different groups. (scale bar: 50 μm) (n = 3 independent biological samples) (**g**) Scheme of multi-pronged ROS amplification in vivo. (1:Control; 2:ZnPP@FOS; 3:ZnPP@FOS+Laser; 4:FQOS; 5:ZnPP@FQOS; 6:ZnPP@FQOS+Laser). i.v. injection, intravenous injection; Bcl-xL, B-cell lymphoma-extra large; HIF−1α, hypoxia-inducible factor−1α. Data are presented as means ± SD. Statistical significance was determined using two-tailed Student's t-test for pairwise comparisons, and one-way ANOVA analysis of variance for multiple groups. p values > 0.05 were considered non-significant, p values < 0.05 were considered statistically significant. Source data are provided as a Source Data file.

blotting. As shown in Fig. 6e, the expression of HO-1 is reduced in the ZnPP@FOS, ZnPP@FOS+Laser, ZnPP@FQOS, and ZnPP@FQOS+Laser groups. The above results demonstrate that a multi-pronged ROS amplification strategy mediated by CAFs remodeling is achieved at the molecular level in vivo. To verify whether laser irradiation alone produces a tumor therapeutic effect, we characterized the tumor tissues accordingly (Supplementary Fig. 43). The results show that the laser irradiation group exhibits the same trend as the control group, with no significant apoptosis and no protein down-regulation trend in the tumor tissues, while the ZnPP@FQOS+Laser group exhibits a good therapeutic effect, which demonstrates the low impact on treatment efficacy under laser irradiation alone. In addition, ROS levels in tumor tissues from different treatment groups were monitored by DCFH-DA staining of pathology sections analysis. As shown in Fig. 6f and Supplementary Fig. 44, compared with the control group, the ZnPP@FOS group shows weak red fluorescence, while the fluorescence intensity of the ZnPP@FOS+Laser group or the FQOS group is a little stronger. The fluorescence intensity of the ZnPP@FQOS group is strengthened again, and the ZnPP@FQOS+Laser group shows the strongest fluorescence. This is mainly because that ROS in the tumor site is gradually amplified in various ways (Fig. 6g). Specifically, ZnPP@FOS amplifies intratumor ROS once by downregulating HO-1 expression; ZnPP@FOS +Laser and FQOS amplify ROS twice by down-regulating HO-1 expression, generating $^1O_2$ and relieving hypoxia as well as inducing apoptosis; ZnPP@FQOS amplifies ROS third time by down-regulating HO-1 expression, relieving hypoxia and inducing apoptosis; ZnPP@FQOS+Laser, then, gathers the features of ZnPP@FOS+Laser and FQOS, which amplifies ROS four times by down-regulating HO-1 expression, generating $^1O_2$, relieving hypoxia, inducing apoptosis, and ultimately forming a ROS bomb. All these results fully demonstrate that ZnPP@FQOS is capable to realize a multi-pronged ROS amplification mediated by CAFs remodeling in vivo.

In order to explore the specific implementation of CAFs remodeling, we analyzed the percentage of CAFs in TME after different treatments using flow cytometry. As shown in Fig. 7a, b, the percentage of the population of CAFs in Que-doped FQOS, ZnPP@FQOS, and ZnPP@FQOS+Laser groups is slightly reduced, where the percentage of the population of CAFs in ZnPP@FQOS+Laser group is reduced from 36.73% to 8.50% compared to the control group. The results reveal that Que-doped nanomedicines are able to decrease the population of CAFs in TME to some extent. Since FAP-α is a signature marker indicating the fibrotic progression of CAFs, we evaluated the population of FAP-α^+ CAFs in TME using flow cytometry (Supplementary Figs. 45, 46). The population of FAP-α^+ CAFs is substantially reduced

https://doi.org/10.1038/s41467-024-55658-0

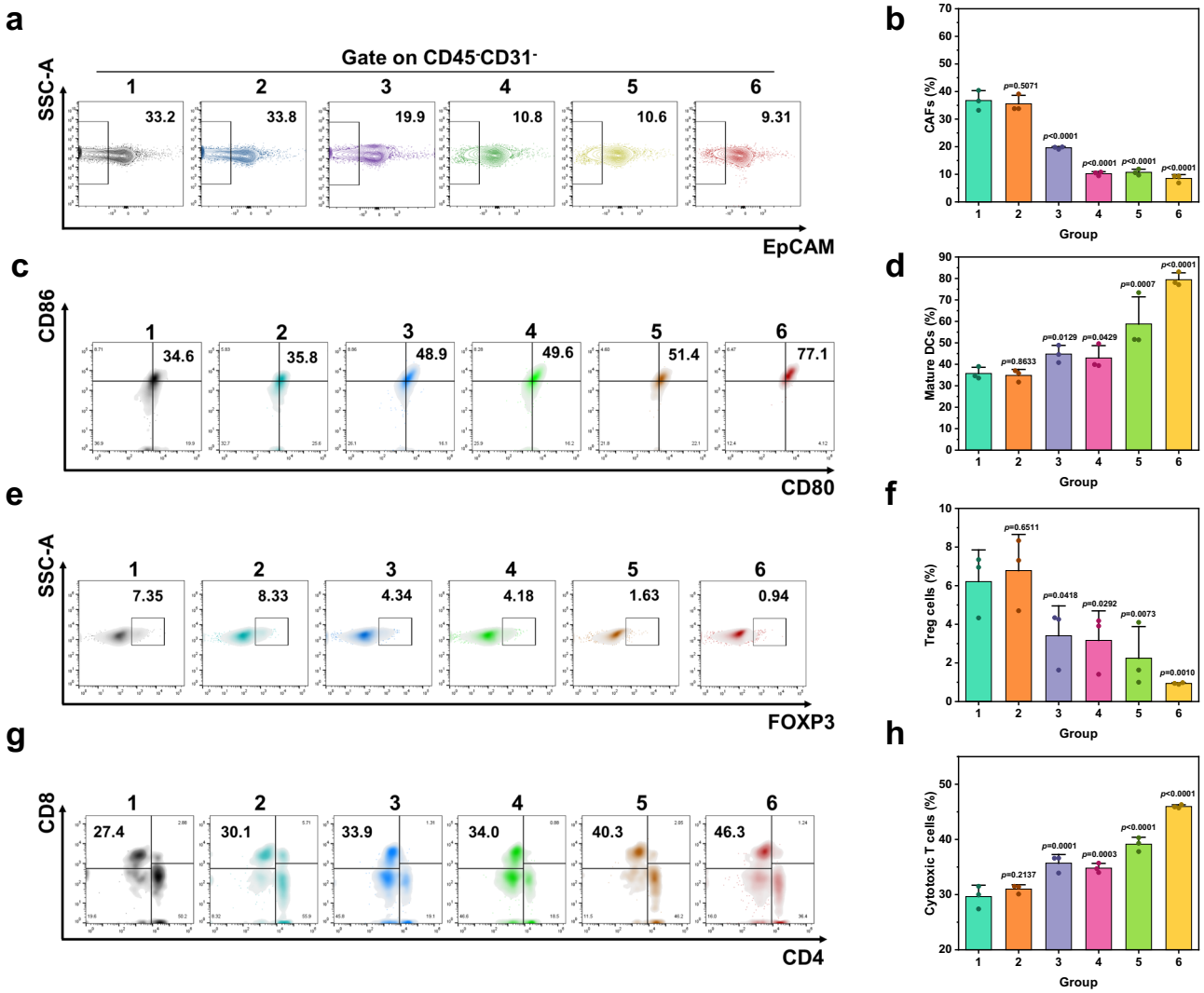

Fig. 7 | In vivo immune response performance of ZnPP@FQOS for fibroblasts-rich KP tumor. a Flow cytometry analysis of the population of EpCAM$^-$CD45$^-$CD31$^-$ CAFs sorting of tumors in mice with different treatments. **b** Corresponding quantification of the population of EpCAM$^-$CD45$^-$CD31$^-$ CAFs with different treatments. (n = 3 independent biological samples) **c** Flow cytometry of CD80$^+$CD86$^+$ mature DCs sorting of spleen in mice with different treatments. **d** Corresponding quantification of the population of CD80$^+$CD86$^+$ mature DCs with different treatments. (n = 3 independent biological samples) **e** Flow cytometry of CD3$^+$Foxp3$^+$ T (Treg) cells sorting of tumor in mice with different treatments. **f** Corresponding quantification of the population of CD3$^+$Foxp3$^+$ T (Treg) cells with different treatments. (n = 3 independent biological samples) **g** Flow cytometry of CD3$^+$CD8$^+$ T (CTLs) cells sorting of tumor-draining lymph nodes in mice with different treatments. **h** Corresponding quantification of the population of CD3$^+$CD8$^+$ T (CTLs) cells with different treatments. (n = 3 independent biological samples) (1:Control; 2:ZnPP@FOS; 3:ZnPP@FOS+Laser; 4:FQOS; 5:ZnPP@FQOS; 6:ZnPP@FQOS+Laser) Data are presented as means ± SD. Statistical significance was determined using two-tailed Student's t-test for pairwise comparisons, and one-way ANOVA analysis of variance for multiple groups. p values > 0.05 were considered non-significant, p values < 0.05 were considered statistically significant. Source data are provided as a Source Data file.

after ZnPP@FQOS+Laser treatment, which is in accordance with the results of western blotting analysis shown in Fig. 6e. These results indicate that remodeling of CAFs achieved by down-regulation of fibrosis-associated proteins as well as a certain amount of CAFs killing is successfully induced in vivo. In addition, our multi-pronged ROS amplification strategy could enhance tumor immunogenicity and reverse immunosuppressive TME in vivo by promoting DCs maturation, Treg cells reduction, and cytotoxic T cells (CTLs) activation (Supplementary Fig. 47), which was confirmed by flow cytometry of single-cell suspensions of tumor tissue, spleen and draining lymph nodes from mice after different treatments (Supplementary Fig. 48). The maturation of DCs in the spleens of mice is increased substantially from 35.73% to 79.43% (2.22 times) after treatment with ZnPP@FQOS compared to the control group, indicating that nanomedicine-induced cell death promoted the abundance of mature DCs-dominant APCs (antigen-presenting cells) (Fig. 7c, d). Meanwhile, flow cytometry results show that Treg cells in the tumor decreased from 6.21% to 0.94% (6.61 times) (Fig. 7e, f), and CTLs infiltrating in the tumor-draining lymph nodes increase from 29.63% to 45.97% (1.55 times) (Fig. 7g, h), verifying that a robust host-specific CTLs response is induced in which tumor cell fragments are activated as antigens. In addition, nanomedicine-triggered multi-pronged ROS amplification group releases approximately 6.28 times and 4.46 times higher pro-inflammatory cytokine tumor necrosis factor α (TNF-α) and interferon γ (IFN-γ) compared to the control group, respectively (Supplementary Figs. 49, 50), which demonstrates that ZnPP@FQOS could remodel the immunosuppressive TME and promote systemic immune response.

In vivo immunotherapy of ZnPP@FQOS combined with anti-PD-L1

The TME in pancreatic cancer is highly immunosuppressive, typically known as immunologically "cold" tumors, hence targeting and

https://doi.org/10.1038/s41467-024-55658-0

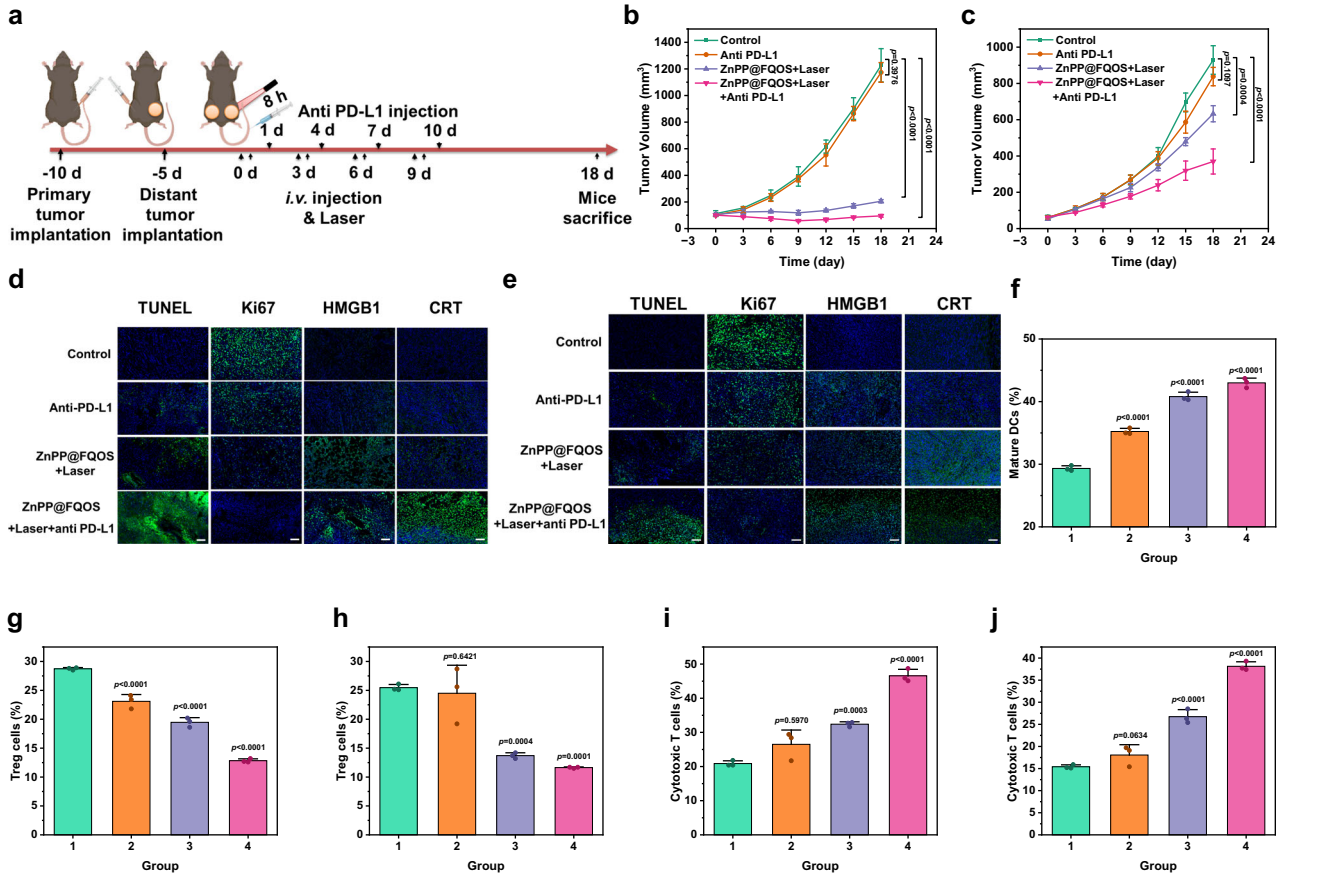

Fig. 8 | In vivo photodynamic-immunotherapy of ZnPP@FQOS combined with anti-PD-L1 for fibroblasts-rich Pan02 tumor. a Schematic illustration of the treatment in bilateral fibroblasts-rich Pan02 tumor models. **b** Primary tumor growth curves throughout the treatment. (n = 3 independent biological samples) **c** Distant tumor growth curves throughout the treatment. (n = 3 independent biological samples) **d** TUNEL, Ki67, HMGB1, CRT staining of primary tumors from each group. (scale bar: 50 μm) (n = 3 independent biological samples) **e** TUNEL, Ki67, HMGB1, CRT staining of distant tumors from each group. (scale bar: 50 μm) (n = 3 independent biological samples) **f** Corresponding quantification of the population of $CD80^+CD86^+$ mature DCs from different treatments. (n = 3 independent biological samples) **g** Corresponding quantification of the population of $CD3^+Foxp3^+$ T (Treg) cells in primary tumors from different treatments. (n = 3 independent biological samples) **h** Corresponding quantification of the population of $CD3^+Foxp3^+$ T (Treg) cells in distant tumors from different treatments. (n = 3 independent biological samples) **i** Corresponding quantification of the population of $CD3^+CD8^+$ T (CTLs) cells in primary tumors from different treatments. (n = 3 independent biological samples) **j** Corresponding quantification of the population of $CD3^+CD8^+$ T (CTLs) cells in distant tumors from different treatments. (n = 3 independent biological samples) (1: Control; 2: Anti-PD-L1; 3: ZnPP@FQOS+Laser; 4: ZnPP@FQOS+Laser+anti-PD-L1). Anti-PD-L1, the antibody of programmed death-ligand 1. Data are presented as means ± SD. Statistical significance was determined using two-tailed Student's t-test for pairwise comparisons, and one-way ANOVA analysis of variance for multiple groups. p values > 0.05 were considered non-significant, p values < 0.05 were considered statistically significant. Source data are provided as a Source Data file.

reinstating the immune system of patients through engineered biomaterials offers an attractive therapeutic approach[47,48]. Based on the satisfactory therapeutic effect and the favorable systematic immune response of ZnPP@FQOS against fibroblasts-rich KP tumors, we further established a bilateral tumor model by inoculating both sides of mice with a mixed suspension of Pan02 and TGF-β-activated 3T3 cells to explore the performance of the ZnPP@FQOS combined with anti-PD-L1 on pancreatic cancer treatment. In the experiments, the primary tumor was treated with laser irradiation after administration of the nanomedicine, while the distant tumor was unirradiated (Fig. 8a). During the 18 days treatment, the anti-PD-L1 group shows a weaker therapeutic effect, while the ZnPP@FQOS+Laser group shows a considerably improved therapeutic effect on primary tumors, with a tumor suppression rate of 83.26%, as well as a certain therapeutic effect on distant tumors, which is attributed to Que-induced remodeling of CAFs and consequently the induction of systemic immunity. The ZnPP@FQOS+Laser+anti-PD-L1 group shows the best therapeutic effect, which produces the most good tumor-suppressive effect on both primary and distant tumors, reaching 92.21% and 60.21%, respectively. This distinct abscopal effect indicate that the anti-tumor immune response to anti-PD-L1 is significantly improved after ZnPP@FQOS-mediated multi-pronged ROS amplification (Fig. 8b, c). Correspondingly, the survival rate of mice in ZnPP@FQOS+Laser+anti-PD-L1 group is prolonged compared to the other groups (Supplementary Fig. 51). The blood indexes and liver&kidney function of the other three groups treated with different nanomedicines remain similar to the control group (Supplementary Figs. 52, 53), suggesting that co-administration of nanomedicine with anti-PD-L1 has no significant side effect in mice. Further immunofluorescence analysis (TUNEL and Ki-67) of the primary and distant tumor tissues shows that the ZnPP@FQOS+Laser+anti-PD-L1 group considerably enhances cell death characteristics and inhibits cell proliferation compared to the other groups (Fig. 8d, e). PDT-induced cancer immune activation is usually mediated by damage-associated molecular patterns (DAMPs), including surface-exposed calcium reticulocyte calpain (CRT) and high mobility group box 1 (HMGB1), and thus we examined the expression levels of CRT and HMGB1 after different treatments (Fig. 8d, e). Immunofluorescence staining results show higher CRT and HMGB1

exposure in primary tumors of ZnPP@FQOS+Laser and ZnPP@FQOS +Laser+anti-PD-L1 groups; however, the fluorescence intensities of CRT and HMGB1 in the distant tumors are only slightly elevated, indicating that primary tumors receive the photodynamic therapy effect provided by laser irradiation while distant tumors do not. These results demonstrate that PDT contribute to the enhancement of the immune response to the primary tumor.

To further elucidate the underlying immunological mechanisms, we performed flow cytometry analysis of immune cells from primary tumors, distant tumors and spleens of mice (Supplementary Fig. 54). Mature DCs in the spleen were first estimated (Fig. 8f and Supplementary Fig. 55), and the highest level of $CD80^+$ $CD86^+$ DCs (43.0%) is observed in the spleen of the ZnPP@FQOS+Laser+anti-PD-L1 group. As shown in Fig. 8g, h and Supplementary Figs. 56, 57, the percentage of $Foxp3^+$ Tregs in both primary tumors and distant tumors of the ZnPP@FQOS+Laser+anti-PD-L1 group is the lowest, i.e. 12.83% and 11.63%, respectively. The percentage of infiltrating $CD3^+CD8^+$ cytotoxic T cells at primary and distant tumor sites is substantially increased in the ZnPP@FQOS+Laser+anti-PD-L1 group, reaching 46.57% and 38.13%, respectively (Fig. 8i, j and Supplementary Figs. 58, 59). In addition, the serum level of TNF-α and IFN-γ is considerably elevated nearly 4.63 and 14.71 times in the ZnPP@FQOS+Laser+anti-PD-L1 group compared with the control group, respectively (Supplementary Figs. 60, 61). These results suggest that ZnPP@FQOS-mediated remodeling of CAFs and induced multi-pronged amplification of intratumoral ROS, contribute to the reversal of the severely immunosuppressive microenvironment in pancreatic cancer, stimulate systemic immunity and thus improve the efficacy of PDT immunotherapy through the synergistic combination with anti-PD-L1.

Discussion

In summary, we have developed a TME-responsive hybrid organosilica micelle loaded with hydrophilic Que and hydrophobic ZnPP simultaneously, as a nanomedicine (named as ZnPP@FQOS) to enable efficient treatment of fibroblasts-rich tumors, stimulate systemic immunity, and further enhance anti-PD-L1-based immunotherapy for highly immunosuppressive pancreatic cancer. With the dual stimulation of weak acidity of TME and excess GSH in tumor cells, the as-synthesized nanomedicine could sequentially release Que and ZnPP. The favorable efficacy of ZnPP@FQOS for tumor therapy has been demonstrated to derive from the progressive multi-pronged ROS amplification due to the remodeling of CAFs, inducing apoptosis of tumor cells, down-regulation of the anti-oxidative stress marker HO-1, and the generation of large quantities of $^1O_2$ under laser irradiation. Consequently, the nanomedicine not only activates systemic immunity, but also enhances the anti-PD-L1 response in mice, thereby reversing the immunosuppressive microenvironment and ultimately achieving a remarkably high-efficacy tumor therapy. This CAFs remodeling-based ROS amplification strategy provides insights in designing the nanomedicine for efficient tumor therapy.

Methods

Ethical statement

All research complied with all relevant ethical regulations: for the mice with a single tumor, the volume of the tumor (measured by $(L \times W^2)/2$) must not exceed 2000 mm^3, and the length must not exceed 20 mm. For the mice bearing with two tumors, which are grown on contralateral flanks on one animal, the size of these should be less and should not exceed the maximum burden of a single tumor. Animal experiments were executed according to the protocol approved by the Laboratory Animal Management Committee of East China University of Science and Technology (approval number: ECUST-2020-04001). C57BL/6 mice (female, 6-week-old) were purchased from Shanghai JieSiJie Laboratory Animal Co., Ltd.. The rearing and storage of mice were carried out in a standard laboratory animal room. All mice (3–5 mice per cage) were housed in a specific pathogen-free environment with a light cycle of 12 h:12 h at a temperature of 23 °C and a humidity of 50%.

Materials and reagents

Pluronic F127 ($PEO_{100}PPO_{65}PEO_{100}$, where PEO represents polyethyleneoxide and PPO represents polypropyleneoxide) and glutathione (GSH) were purchased from Sigma-Aldrich. (3-Mercaptopropyl)trimethoxysilane (MPTMS) was purchased from TCI. Zinc protoporphyrin (ZnPP) was purchased from Alfa Aesar. Quercetin (Que) was purchased from Medchem Express. 1,3-Diphenylisobenzofuran (DPBF), ethanol, NH_4OH, dimethyl sulfoxide (DMSO) and 2,2,6,6-tetramethylpiperidine (TEMP) were purchased from Adamas. All chemicals were used as received without further purifications.

Characterization

The sizes and Zeta potentials of samples were measured at 25 °C with a Malvern Zetasizer (Nano ZS, Malvern, UK). The morphologies of samples were measured by JEM-2100 TEM (JEOL, Japan). UV-visible spectra of samples were measured by a UV-visible spectrophotometer (Shimadzu, UV-3600, Japan). Fourier transform infrared (FT-IR) spectra were measured on Nicolet iS50 spectrometer. Raman spectra were measured on Laser Micro-Raman Spectrometer with 785 nm laser (Renishaw, UK). Electron spin resonance was measured with a Bruker EMX-8/2.7 (100G-18 KG) spectrometer. Confocal laser scanning microscopy (CLSM) images were recorded by Leica Microsystems (LEICA TCS SP8, German). Flow cytometry were used to test the cellular uptake and cell apoptosis (BD Accuri C6, USA).

Synthesis of ZnPP@FQOS

The preparation route was adapted from our previous work[32–34]. Briefly, F127 (600 mg) and ZnPP (10 mg) were added to a 250 ml round bottom flask and dissolved in ethanol (15 ml). The ethanol was then evaporated at 45 °C to obtain a thin film. The film was re-dissolved in water (15 mL) at 45 °C to obtain an aqueous solution of ZnPP@F127 micelles. Subsequently, NH_4OH (100 μL) and Que (10 mg) were added sequentially to the solution. After 1 min when Que was completely dissolved, MPTMS (300 μL) was added to the solution. The obtained solution was stirred at room temperature for 24 h, added into a dialysis bag with a molecular weight cut-off (MWCO) of 8000–14000 and dialyzed with ultra-pure water to remove impurities. Finally, ZnPP@FQOS solution was collected from the dialysis bag.

The synthesis of FOS was similar to the process mentioned above except that ZnPP and Que were not added.

The synthesis of ZnPP@FOS and FQOS was similar to the process mentioned above except that Que or ZnPP were not added.

The loading content of ZnPP was determined by re-dispersing the freeze-dried ZnPP@FOS micelle in DMSO and measuring the absorbance at 585 nm by UV-Vis, which was then compared with the predetermined standard curve of ZnPP in DMSO solution. Based on the pre-determined standard curve, the freeze-dried FQOS micelles were re-dispersed in DMSO and the loading content of Que was determined by the same method.

In vitro drug release

To characterize the pH/GSH responsive release property of ZnPP@FQOS, the FQOS solution was added to the dialysis bag and immersed into PBS buffer solution (30 mL, containing 3% DMSO) at different pH value (5.7, 6.5, 7.4) and incubated at 37 °C with a shaker. At indicated time points, 1 mL of dialysis medium was removed and its UV-Vis absorption spectrum was measured to determine the concentration of Que, and 1 mL of freshly prepared dialysis medium was replenished. Similarly, ZnPP@FOS solution was added to the dialysis bag and immersed into PBS buffer solution (30 mL, containing 3% DMSO) with different GSH concentration (0, 2 mM, 10 mM) incubated

at 37 °C with a shaker. The cumulative release property was measured by the same method mentioned above.

To characterize the pH/GSH-dual responsive release property of ZnPP@FQOS, the ZnPP@FQOS solution was added to the dialysis bag and immersed into PBS buffer solution (30 mL, containing 3% DMSO) with different pH value (5.7, 6.5, 7.4) and GSH concentration (0, 2 mM, 10 mM). The cumulative release property was measured by the same method mentioned above.

Evaluation of $^1O_2$ generation

The generation of singlet oxygen ($^1O_2$) was detected via a chemical oxidation method based on DPBF, which can irreversibly react with $^1O_2$ resulting in a decrease of the UV-vis absorbance. Specifically, 100 μL DPBF (1 mM) was mixed with 4 mL ZnPP@FOS, FQOS, ZnPP@FQOS aqueous solution (300 μg/mL), respectively by sonication in the dark. Then 20 μL H_2O_2 (30%) was added to the mixed solution. The mixed solution was irradiated under Laser (660 nm, 300 mW cm^{-2}) for 5 min. The change in absorption was recorded. The pure DPBF group was also recorded as a control.

For ESR measurement, 2,2,6,6-tetramethylpiperidine (TEMP) was used as a spin trapper for the detection of $^1O_2$. 4 mM TEMP was added into the sample solution, which was then irradiated under 660 nm laser and filtrated through a 0.22 μm NY membrane before the measurement.

Cell culture

The KP, 3T3 and MEF cells were obtained from ATCC (USA). The Pan02 cells were purchased from BeNa Culture Collection (Henan, China). These cells were cultured in normal Dulbecco's modified eagle medium (DMEM) containing 10% fetal bovine serum (FBS, Gibco, South America) and 1% penicillin/streptomycin. Cell cultures were maintained in an incubator at 37 °C in a humidified atmosphere with 5% CO_2.

Cell uptake

Pan02 and 3T3 cells were incubated in 6-well plates for 24 h, and 3T3 cells were pre-activated with 25 ng/mL TGF-β (Yeasen Biotechnology (Shanghai) Co., Ltd.). After 24 h of adhesion, the Pan02 and TGF-β activated 3T3 cells were treated with medium containing ZnPP@FQOS for different times (1, 2, 4, 8 and 12 h). ZnPP@FQOS was removed and the cells were washed for 3 times with PBS. Then 1 mL Hoechst 33342 was added, and cells were darkly stained for about 15 min. Subsequently, Hoechst 33342 was removed and the cells were washed for 3 times with PBS. Finally, 1 mL PBS was added and cells were imaged by Confocal Laser Scanning Microscopy (CLSM).

Free ZnPP; ZnPP@FOS; ZnPP@FOS+Free Que and ZnPP@FQOS were incubated with Pan02 or TGF-β activated 3T3 cells for 4 h to investigate the cellular uptake of different nanomedicines. CLSM imaging steps are the same as above.

Pan02 cells were inoculated in 6-well plates at a density of 1×10^5 cells/well for 24 h for adherent growth, and then the medium was replaced with new culture medium containing ZnPP@FQOS in advance of the expected time point. Finally, the cells were digested with trypsin at the same time, centrifuged and washed for 3 times with PBS. After removing impurities such as unphagocytosed ZnPP@FQOS and trypsin, the collected Pan02 cells were re-suspended in 0.5 mL of PBS and examined by flow cytometry.

In vitro tumor penetration of multi cellular tumor spheroids (MCTS)

To establish the MCTS model, 6×10^3 KP cells and 2×10^3 TGF-β-activated 3T3 cells were co-transplanted into a Nunclon Sphera 6-well plate and incubated at 37 °C for 8 d, and the medium was half-changed every 2 days. When the diameter reached about 120 μm, they were ready for further experiments. To study tumor penetration, the MCTSs were treated by Free ZnPP, ZnPP@FOS, ZnPP@FOS (pH=6.5), ZnPP@FOS+Free Que, ZnPP@FQOS and ZnPP@FQOS (pH=6.5), respectively. After incubation for 12 h, the MCTSs were washed for 3 times with PBS and imaged by CLSM.

In vitro western blotting analysis

KP or 3T3 cells were incubated in 6-well plates (1×10^5 cells/well) for 24 h, digested and collected after administering with the indicated treatment for 24 h. The cells were lysed with EDTA-free cell lysate containing complete protease inhibitors, and then boiled with Laemmli sample buffer for 5 min. Subsequently, the cell lysate (20 mg protein) was separated on 12% SDS-PAGE, transferred to a PVDF membrane, and blocked with TBST containing 5% BSA (1:1000 dilution) before incubating with the primary antibody (overnight) and the secondary antibody (1:3000 dilution) at room temperature for 2 h. Finally, the ECL chemiluminescence kit (Beyotime, P0018FS) was used for western blotting analysis.

In vitro immunofluorescence image of α-SMA and HO-1

KP or 3T3 cells were incubated in 12-well plates with dedicated cell climbing film (5×10^4 cells/well) for 24 h, and administered with indicated treatment for 24 h. Afterwards, the KP or 3T3 cells were fixed with 4% paraformaldehyde and permeabilized with 0.2% Triton-X-100. Next, the KP or 3T3 cells were blocked with 5% bovine serum albumin (BSA) and further incubated with primary antibodies (α-SMA or HO-1 antibody) and Alexa Fluor 488 or Alexa Fluor 568 conjugated secondary antibody. Finally, CLSM was used for immunofluorescence imaging.

In vitro ROS generation

To evaluate the intracellular ROS level, KP and 3T3 mixed cells (1×10^5 cells/well) were seeded in 6-well plates, which were then administered with indicated treatment for 24 h. Next, the medium was replaced by a serum-free medium with 10 mM of 2′,7′-dichlorofluorescin diacetate (DCFH-DA). After a further 15 min of incubation, the cells were washed with PBS and irradiated by a 660 nm laser (300 mW/cm^2) or shielded in dark. Finally, the cells were then observed by CLSM.

The intracellular $^1O_2$ level was also evaluated. KP and 3T3 mixed cells were seeded in 6-well plates at a density of 1×10^5 cells/well, and then administered with indicated treatment for 24 h. Next, the medium was replaced by a serum-free medium with 2.0 μM of SOSG. After a further 30 min of incubation, the cells were washed with PBS and irradiated by a 660 nm laser (300 mW/cm^2) or shielded in dark. Finally, the cells were then observed by CLSM.

In vitro mitochondrial membrane potential detection

KP and 3T3 mixed cells were seeded in 6-well plates (1×10^5 cells/well) for 24 h, which were then administered with indicated treatment for 24 h. Next, 500 μL of mitochondrial membrane potential reagent of JC-1 solution was added into the dishes. After a further 20 min of incubation, the cells were washed with PBS and irradiated by a 660 nm laser (300 mW/cm^2) or shielded in dark. Finally, the cells were then imaged by CLSM.

In vitro cytotoxicity measurements

The cytotoxicity was measured by a standard Cell Counting Kit-8 assay. The KP, Pan02, 3T3 and MEF cells were seeded into 96-well plates at an initial density of 5×10^3 cells/well. After 24 h of adherence, the cells were administered with indicated treatment. After 24 h of incubation, the medium was removed and the CCK-8 assay was used to quantify cell viabilities.

KP cells were incubated in 6-well plates at an initial density of 1×10^5 cells/well for 24 h. After administering with the indicated treatment for 24 h, cells were trypsinized, washed, and resuspended in 0.5 mL of binding solution, followed by the incubation with the Annexin V-FITC/PI Apoptosis Detection Kit in dark for 15 min.

Afterwards, the KP cells were washed with PBS for 2 times and analyzed immediately using a flow cytometer (BD Accuri C6, USA).

For the live-dead cell staining experiment, KP cells were incubated in 6-well plates at an initial density of 1×10^5 cells/well for 24 h. After administering with the indicated treatment for 24 h, the medium was replaced with fresh medium and further stained according to the instructions of Calcein/PI Live/Dead Viability Assay Kit. Finally, the cells were then imaged by CLSM.

In vitro DC2.4 cell maturation assay

KP and 3T3 mixed cells were cultured in a 6-well plate, and then treated with PBS, ZnPP@FOS, ZnPP@FOS+Laser, FQOS, ZnPP@FQOS, ZnPP@FQOS+Laser (ZnPP dose: 7.724 mg/L, Que dose: 10 mg/L) at 37°C overnight. The supernatant of these KP and 3T3 mixed cells was collected and then incubated with DC2.4 cells (2×10^6 cells per well in a 6-well plate). After a 24-hour incubation, DC2.4 cells were digested by trypsin and stained with APC-CD80, BV421-CD86, and FITC-CD11c antibodies for 30 min at 4°C. These cells were washed three times with FACS buffer before being analyzed by the flow cytometer (Cytek Aurora, USA).

In vivo biosafety study

C57BL/6 mice (female, 6-week-old) were divided into 2 groups of 5 mice each, and ZnPP@FQOS (Que dose: 10 mg/kg) was injected intravenously via tail vein into one group of mice. During the period of 18 days healthy monitoring, the body weight of mice in each group was measured and recorded every 3 days. 18 days later, the mice were sacrificed and the major organs (heart, liver, spleen, lung and kidney) of the two groups were collected and sliced for Hematoxylin & Eosin (H&E) staining. Meanwhile, whole blood as well as serum was collected for the evaluation of blood index and liver & kidney function (hematology and blood biochemistry index).

In vivo biodistribution study

3×10^6 KP and 1×10^6 TGF-β-activated 3T3 mixed cell suspension was subcutaneously injected into the back of the hind leg to establish fibroblasts-rich KP tumor-bearing C57BL/6 mice (female, 6-week-old) model. The mice were then randomly divided into 3 groups of 5 mice each (Free ZnPP group, ZnPP@FOS group, ZnPP@FQOS group) (ZnPP dose: 3.862 mg/kg, Que dose: 5 mg/kg). The in vivo fluorescence images were recorded at 0, 3, 6, 12, 24, and 36 h post-injection via an in vivo imaging system (IVIS Lumina XRMS Series III, PerkinElmer, USA). At 36 h post-injection, mice were sacrificed, and the heart, liver, spleen, lung, kidney and tumor were collected and processed for ex vivo imaging. The tumor tissues were sectioned and further used for immunofluorescence analysis.

In vivo photodynamic therapy and immune response

Fibroblast-rich KP tumor C57BL/6 mice (female, 6-week-old) model was established as described above. Mice were randomly divided into 6 groups of 5 mice each: 1. Control; 2. ZnPP@FOS; 3. ZnPP@FOS +Laser; 4. FQOS; 5. ZnPP@FQOS; 6. ZnPP@FQOS+Laser (ZnPP dose: 3.862 mg/kg, Que dose: 5 mg/kg). Treatments were initiated when the average tumor size reached approximately 50 mm^3. Mice were intravenously injected with different treatments at day 0,3,6, and 9 and the laser was performed (660 nm, 300 mW cm^{-2} and 5 min) at 8 h after intravenous injection in group 3 and group 6. The tumor sizes and body weights were monitored every 3 days. After 18 days, mice were sacrificed and the tumors and major organs were collected for histopathological section analysis, western blotting, immunofluorescence and IHC analysis. Meanwhile, the spleen was excised and prepared for single-cell suspension, followed by CD11c/80/86 staining for analyzing DC maturation by flow cytometry. The tumor tissues and tumor-draining lymph nodes were also dissected and prepared for single-cell suspension for flow cytometry to analyze $CD3^+$, $CD4^+$ and $CD8^+$ T cells, Treg cells, CAFs and FAP^+CAFs. The whole blood was collected to isolate serum for ELISA analysis of IFN-γ and TNF-α.

In vivo ROS generation

Fibroblast-rich KP tumor-bearing C57BL/6 mice (female, 6-week-old) were randomly divided into the above six groups. When the tumors reached a mean group size of approximately 250 mm^3, the mice were intravenously injected with different treatments (ZnPP dose: 3.862 mg/kg, Que dose: 5 mg/kg) and the laser was performed (660 nm, 300 mW cm^{-2} and 5 min) at 8 h after intravenous injection in group 3 and group 6. Mice were sacrificed 24 h after irradiation, and their tumor tissues were dissected and immediately frozen in a refrigerator (−60 °C) for making sections. Then the DCFH-DA assay was used for ROS staining of tumor tissues.

In vivo photodynamic-immunotherapy

Fibroblast-rich Pan02 bilateral tumor-bearing C57BL/6 mice (female, 6-week-old) model was established by subcutaneously injecting 3×10^6 Pan02 and 1×10^6 TGF-β-activated 3T3 mixed cell suspension on the back of the both side of the hind legs. Fibroblast-rich Pan02 tumor-bearing mice at both right (primary tumor) and left (distant tumor) back of the hind legs were randomly divided into 4 groups: 1. Control; 2. Anti PD-L1; 3. ZnPP@FQOS+Laser; 4. ZnPP@FQOS+Laser+anti PD-L1. Treatments were initiated when the average size of primary tumor reached approximately 100 mm^3 and tumor-bearing mice were subjected to different treatment over a period of 18 days. After 8 h post-intravenous injection of different solution on day 0, 3, 6, and 9, the primary tumors were irradiated by laser (660 nm, 300 mW cm^{-2}) for 5 min. The anti PD-L1 (dose: 75 μg/mouse) was intraperitoneally injected on day 1, 4, 7 and 10. The tumor sizes were monitored every 3 days. After 18 days, 3 mice in each group were sacrificed and the primary and distant tumors were removed for immunofluorescence analysis. Meanwhile, the spleen was excised and prepared for single-cell suspension, followed by CD11c/80/86 staining for analyzing DC maturation by flow cytometry. The primary and distant tumor tissues were also dissected and prepared for single-cell suspension for flow cytometry for analyzing $CD3^+$, $CD4^+$ and $CD8^+$ T cells, Treg cells. The whole blood as well as serum was collected for the detection of blood index, liver & kidney function and ELISA analysis of IFN-γ and TNF-α. The remaining mice were used to observe long-term survival. When the tumors reached 2000 mm^3, the mice were sacrificed according to appropriate ethical guidelines.

In vivo flow cytometry and analysis

The flow cytometry of the tumor-draining lymph nodes, spleens, and tumors was operated on the flow cytometer. Tumor-draining lymph nodes, spleens, and tumors were dissected and cut into small pieces. Afterwards, tumors were digested with collagenase (Sigma, C5138) and DNase (Sigma, DN25) for the preparation of single-cell suspension with filter. Fc receptors were blocked with incubation of CD16 + CD32 antibody at room temperature. Subsequently, LIVE/DEAD Fixable Violet Dead Cell Stain Kit (Invitrogen), CD45-BV605, CD3-FITC, CD8-Percep-cy5.5, CD4-APC-cy7, CD11c-BV785, CD80-APC, CD86-AF700 antibodies were used to stain the surface markers of lymphocytes, before FOXP3-PE staining at 4 °C for 30 min with Foxp3 / Transcription Factor Staining Buffer Set (eBioscience) in terms of the user guides. Extraction of CAFs from tumor tissue was performed according to the reference methods[49]. To isolate CAFs and FAP^+CAFs, cells in suspension were stained with an antibody mixture containing anti-EpCAM-PE, anti-CD31-APC, anti-CD45.2-FITC, anti-CD29-PE-Cy7 and anti-FAPα-BV421 for flow cytometry. All purchased antibodies except FAPα were conjugated with fluorescent dyes. Anti-FAPα antibody was conjugated with fluorescent dye Goat Anti Rabbit IgG H&L (Alexa Fluor 405). The following isotype control antibodies for each CAF marker were used: iso-anti-CD29 and isoanti-FAPα. Gating included $EpCAM^-$,

$CD45^-$, $CD31^-$ to remove epithelial ($EpCAM^+$), hematopoietic ($CD45^+$) and endothelial ($CD31^+$)[50].

Statistical analysis
Statistical analyses were conducted using OriginPro 2024, Graphpad Prism 9.5, and IBM SPSS Statistics 27 software. All flow cytometry data were analyzed on Flowjo V10 software. All mean fluorescence intensities were calculated by ImageJ. The samples/animals were allocated to experimental groups and processed randomly.

Reporting summary
Further information on research design is available in the Nature Portfolio Reporting Summary linked to this article.

Data availability
All data of this study are available in the main manuscript and its Supplementary Information. Any additional requests for information can be directed to, and will be fulfilled by, the corresponding authors. Source data are provided with this paper.

References

1. Zhang, Q. Y., Luo, Q. H., Liu, Z. M., Sun, M. C. & Dong, X. Nano-ROS-generating approaches to cancer dynamic therapy: Lessons from nanoparticles. *Chem. Eng. J.* **457**, 141225 (2023).
2. Trachootham, D., Alexandre, J. & Huang, P. Targeting cancer cells by ROS-mediated mechanisms: a radical therapeutic approach? *Nat. Rev. Drug Discov.* **8**, 579–591 (2009).
3. Harris, I. S. et al. Glutathione and thioredoxin antioxidant pathways synergize to drive cancer initiation and progression. *Cancer Cell* **27**, 211–222 (2015).
4. Ryter, S. W., Alam, J. & Choi, A. M. K. Heme oxygenase-1/carbon monoxide: from basic science to therapeutic applications. *Physiol. Rev.* **86**, 583–650 (2006).
5. Fang, J., Seki, T. & Maeda, H. Therapeutic strategies by modulating oxygen stress in cancer and inflammation. *Adv. Drug Deliv. Rev.* **61**, 290–302 (2009).
6. Yu, W. J. et al. Enhanced transcutaneous chemodynamic therapy for melanoma treatment through cascaded fenton-like reactions and nitric oxide delivery. *ACS Nano* **17**, 15713–15723 (2023).
7. Xu, J. et al. Self-Immolative amphiphilic poly(ferrocenes) for synergistic amplification of oxidative stress in tumor therapy. *Angew. Chem. Int. Ed.* **62**, e202303829 (2023).
8. Mai, Z. et al. Carrier-free immunotherapeutic nano-booster with dual synergistic effects based on glutaminase inhibition combined with photodynamic therapy. *ACS Nano* **17**, 1583–1596 (2023).
9. Zhang, W. J., Hu, X. L., Shen, Q. & Xing, D. Mitochondria-specific drug release and reactive oxygen species burst induced by polyprodrug nanoreactors can enhance chemotherapy. *Nat. Commun.* **10**, 1704 (2019).
10. Kraman, M. et al. Suppression of antitumor immunity by stromal cells expressing fibroblast activation protein-alpha. *Science* **330**, 827–830 (2010).
11. Han, X. X. et al. Emerging nanomedicines for anti-stromal therapy against desmoplastic tumors. *Biomaterials* **232**, 119745 (2020).
12. Stylianopoulos, T., Munn, L. L. & Jain, R. K. Reengineering the physical microenvironment of tumors to improve drug delivery and efficacy: from mathematical modeling to bench to bedside. *Trends Cancer* **4**, 292–319 (2018).
13. Nia, H. D. T., Munn, L. L. & Jain, R. K. CANCER Physical traits of cancer. *Science* **370**, eaaz0868 (2020).
14. Stylianopoulos, T. et al. Causes, consequences, and remedies for growth-induced solid stress in murine and human tumors. *P. Natl Acad. Sci. Usa.* **109**, 15101–15108 (2012).
15. Nia, H. T. et al. Solid stress and elastic energy as measures of tumour mechanopathology. *Nat. Biomed. Eng.* **1**, 0004 (2017).
16. Sahai, E. et al. A framework for advancing our understanding of cancer-associated fibroblasts. *Nat. Rev. Cancer* **20**, 174–186 (2020).
17. Seano, G. et al. Solid stress in brain tumours causes neuronal loss and neurological dysfunction and can be reversed by lithium. *Nat. Biomed. Eng.* **3**, 230–245 (2019).
18. Jiang, W. et al. Tumor reoxygenation and blood perfusion enhanced photodynamic therapy using ultrathin graphdiyne oxide nanosheets. *Nano Lett.* **19**, 4060–4067 (2019).
19. Zhang, Z. J. et al. A two-pronged strategy to alleviate tumor hypoxia and potentiate photodynamic therapy by mild hyperthermia. *Biomater. Sci.* **11**, 108–118 (2022).
20. Rhim, A. D. et al. Stromal elements act to restrain, rather than support, pancreatic ductal adenocarcinoma. *Cancer Cell* **25**, 735–747 (2014).
21. Ozdemir, B. C. et al. Depletion of Carcinoma-Associated Fibroblasts and Fibrosis Induces Immunosuppression and Accelerates Pancreas Cancer with Reduced Survival. *Cancer Cell* **25**, 719–734 (2015).
22. Lee, J. J. et al. Stromal response to Hedgehog signaling restrains pancreatic cancer progression. *P. Natl Acad. Sci. Usa.* **111**, E3091–E3100 (2014).
23. Froeling, F. E. & Kocher, H. M. Homeostatic restoration of desmoplastic stroma rather than its ablation slows pancreatic cancer progression. *Gastroenterology* **148**, 849–850 (2015).
24. Chen, X. M. & Song, E. W. Turning foes to friends: targeting cancer-associated fibroblasts. *Nat. Rev. Drug Discov.* **18**, 99–115 (2019).
25. Sherman, M. H. et al. Vitamin D receptor-mediated stromal reprogramming suppresses pancreatitis and enhances pancreatic cancer therapy. *Cell* **159**, 80–93 (2014).
26. Kumar, K. et al. BET inhibitors block pancreatic stellate cell collagen I production and attenuate fibrosis in vivo. *JCI Insight* **2**, e88032 (2017).
27. Jaster, R. et al. Regulation of pancreatic stellate cell function in vitro: biological and molecular effects of all-trans retinoic acid. *Biochem. Pharmacol.* **66**, 633–641 (2003).
28. McCarroll, J. A. et al. Vitamin A inhibits pancreatic stellate cell activation: implications for treatment of pancreatic fibrosis. *Gut* **55**, 79–89 (2006).
29. Masamune, A. et al. Control of activation targeting signal transduction pathways in rat pancreatic stellate cells. *Gastroenterology* **122**, A412–A412 (2002).
30. Chronopoulos, A. et al. ATRA mechanically reprograms pancreatic stellate cells to suppress matrix remodelling and inhibit cancer cell invasion. *Nat. Commun.* **7**, 12630 (2016).
31. Hu, K. L. et al. Quercetin remodels the tumor microenvironment to improve the permeation, retention, and antitumor effects of nanoparticles. *ACS Nano* **11**, 4916–4925 (2017).
32. Niu, D. C. et al. Superstable and large-scalable organosilica-micellar hybrid nanosystem a confined gelation strategy for ultrahigh-dosage chemotherapy. *Nano Lett.* **21**, 9388–9397 (2021).
33. Li, X. L. et al. A "valve-closing" starvation strategy for amplification of tumor-specific chemotherapy. *Adv. Sci.* **9**, 2104671 (2022).
34. Li, X. L. et al. Dual "unlocking" strategy to overcome inefficient nanomedicine delivery and tumor hypoxia for enhanced photodynamic-immunotherapy. *Adv. Healthc. Mater.* **12**, 2202467 (2023).
35. Sun, Q. Q. et al. A Stepwise-confined self-reduction strategy to construct a dynamic nanocatalyst for boosting tumor catalytic therapy. *Chem. Mater.* **35**, 177–188 (2023).
36. Román-Gómez, J. et al. Epigenetic regulation of Wnt-signaling pathway in acute lymphoblastic leukemia. *Blood* **109**, 3462–3469 (2007).
37. Sun, D. D. et al. A cyclodextrin-based nanoformulation achieves co-delivery of ginsenoside Rg3 and quercetin for chemo-immunotherapy in colorectal cancer. *Acta Pharm. Sin. B* **12**, 378–393 (2022).
38. Yang, G. et al. Unique effects of zinc protoporphyrin on HO–1 induction and apoptosis. *Blood* **97**, 1306–1313 (2001).

39. Zheng, R. X. et al. Biodegradable copper-based nanoparticles augmented chemodynamic therapy through deep penetration and suppressing antioxidant activity in tumors. *Adv. Healthc. Mater.* **10**, 2100412 (2021).
40. Cheng, Y. et al. Bismuth sulfide nanorods with retractable zinc protoporphyrin molecules for suppressing innate antioxidant defense system and strengthening phototherapeutic effects. *Adv. Mater.* **31**, 1806808 (2019).
41. Fang, J. et al. antitumor activity of pegylated zinc protoporphyrin:: targeted inhibition of heme oxygenase in solid tumor. *Cancer Res.* **63**, 3567–3574 (2003).
42. Liu, J. J. et al. Biodegradable nanoscale coordination polymers for targeted tumor combination therapy with oxidative stress amplification. *Adv. Funct. Mater.* **30**, 1908865 (2020).
43. Huang, C. H., Chen, X. Y., Xue, Z. J. & Wang, T. Effect of structure: a new insight into nanoparticle assemblies from inanimate to animate. *Sci. Adv.* **6**, eaba1321 (2020).
44. Huo, M. F., Wang, L. Y., Chen, Y. & Shi, J. L. Tumor-selective catalytic nanomedicine by nanocatalyst delivery. *Nat. Commun.* **8**, 357 (2017).
45. Li, X. et al. Reversing insufficient photothermal therapy-induced tumor relapse and metastasis by regulating cancer-associated fibroblasts. *Nat. Commun.* **13**, 2794 (2022).
46. Zhao, X. Z. et al. Penetration cascade of size switchable nanosystem in desmoplastic stroma for improved pancreatic cancer therapy. *ACS Nano* **15**, 14149–14161 (2021).
47. Ho, W. J. & Jaffee, E. M. Disrupting a converging metabolic target turns up the immunologic-heat in pancreatic tumors. *J. Clin. Invest.* **130**, 71–73 (2020).
48. Ho, W. J., Jaffee, E. M. & Zheng, L. The tumour microenvironment in pancreatic cancer - clinical challenges and opportunities. *Nat. Rev. Clin. Oncol.* **17**, 527–540 (2020).
49. Kieffer, Y. et al. Single-cell analysis reveals fibroblast clusters linked to immunotherapy resistance in cancer. *Cancer Discov.* **10**, 1330–1351 (2020).
50. Zhou, H. et al. A tumor-microenvironment-activatable molecular pro-theranostic agent for photodynamic and immunotherapy of cancer. *Adv. Mater.* **35**, 2211485 (2023).

Acknowledgements

This work was financially supported by the National Key Research and Development Program of China (No. 2022YFC2403203, Y.L.), the National Natural Science Foundation of China (No. 22305081, D.Z.), Basic Research Program of Shanghai (No. 21JC1406003, Y.L.), Leading Talents in Shanghai in 2018, the Key Field Research Program (No. 2023AB054, Y.L.), Shanghai Sailing Program (23YF1408600, D.Z.) and the Innovation Program of Shanghai Municipal Education Commission (No. 2023ZKZD33, P.Z.)

Author contributions

Y.L. and J.Z. conceived the project. Y.L., and P.Z. supervised as well as funded the research. Y.L., D.Z., and B.D. revised the manuscript. J.Z. performed most experiments and wrote the original manuscript. C.J. processed and analyzed most of the experiment results. Q.H. assisted in processing the experiment results. X.J. and Y.M. helped with the in vivo fluorescence imaging experiments. S.Wang helped with the transmission electron microscopy image capture, and S.Wan helped with the sacrifice of the mice.

Competing interests

The authors declare no conflict of interest.

Additional information

Supplementary information The online version contains supplementary material available at https://doi.org/10.1038/s41467-024-55658-0.

Correspondence and requests for materials should be addressed to Peng Zhang or Yongsheng Li.

Peer review information *Nature Communications* thanks Kaili Hu, Ji Qi and the other, anonymous, reviewer(s) for their contribution to the peer review of this work. A peer review file is available.